

# Characterising the Impact of Systematic Flat-Fielding Errors In Huntsman Telescope Data

By

**Fergus Longbottom**

A thesis submitted to Macquarie University

for the degree of Master of Research

Department of Astronomy

January 2019



**MACQUARIE**  
University  
SYDNEY · AUSTRALIA

Examiner's Copy



Except where acknowledged in the customary manner, the material presented in this thesis is, to the best of my knowledge, original and has not been submitted in whole or part for a degree in any university.

---

Fergus Longbottom



# Abstract

The Huntsman Telescope is a new facility being commissioned at Siding Spring Observatory in Australia. It consists of an array of Canon telephoto lenses. In order to circumvent the systematic errors known to effect mirror based instruments, the Canon lenses act together as a single refracting telescope. They reduce the scattering of light within the optical path, which allows fainter limiting surface brightness levels to be reached. However, at these low surface brightness levels other sources of systematic error must be carefully investigated and scrutinised. In this thesis I will investigate one of the primary sources of systematic error in low surface brightness imaging, flat fielding uncertainties, and how it impacts the Huntsman Telescope.



# Contents

<b>Abstract</b>	<b>v</b>
<b>Contents</b>	<b>vii</b>
<b>List of Figures</b>	<b>ix</b>
<b>List of Tables</b>	<b>xi</b>
<b>1 Introduction</b>	<b>1</b>
1.1 Background & Significance . . . . .	1
1.1.1 Theory . . . . .	1
1.1.2 Need for Low Surface Brightness Imaging . . . . .	2
1.1.3 Previous Work . . . . .	3
1.2 Observational Issues and Quality Control . . . . .	5
1.3 Flat-Fielding . . . . .	7
1.4 Structure of Thesis . . . . .	9
<b>2 Methods</b>	<b>11</b>
2.1 Observing with the Huntsman Telescope . . . . .	12
2.2 Preparation of Master Darks . . . . .	15
2.3 Preparation of Flat-Field Data . . . . .	16
2.3.1 Twilight Flat-Data Preparation . . . . .	16
2.3.2 Night Flat-Data Preparation . . . . .	16
2.4 Data Collection & Data Degradation . . . . .	18
2.5 Quality Control Diagnostic . . . . .	21

---

<b>3</b>	<b>Flat-Fielding Expectations, Strategy and Quality Control</b>	<b>23</b>
3.1	Theory and Expectations . . . . .	23
3.1.1	Dome Flats . . . . .	25
3.1.2	Night Flats . . . . .	25
3.1.3	Twilight Flats . . . . .	26
3.2	Flatfield Data Quality Control . . . . .	27
3.2.1	Twilight Flat Quality Control . . . . .	27
3.2.2	Night Flat Quality Control . . . . .	31
<b>4</b>	<b>Flat-Field Data Characterisation</b>	<b>35</b>
4.1	Twilight Flat Characterisation . . . . .	35
4.1.1	Residual Circular Feature . . . . .	38
4.2	Night Flats Characterisation . . . . .	41
<b>5</b>	<b>Discussion and Conclusions</b>	<b>45</b>
5.1	Twilight Flats . . . . .	45
5.2	Night Flats . . . . .	47
5.3	Future Work . . . . .	49
<b>A</b>	<b>Appendix</b>	<b>51</b>
	<b>References</b>	<b>61</b>

# List of Figures

2.1	Demonstration of dynamic twilight flat exposure time estimation. . . . .	14
2.2	Example of Huntsman dark current. . . . .	15
2.3	Illustration of aggressive source masking procedure. . . . .	17
2.4	Examples of bad quality data. . . . .	19
3.1	The impact of flat-field error on surface brightness depth limit. . . . .	24
3.2	Reference morning and evening master flats for a single camera and filter. .	28
3.3	Distribution of Quality Control scores. . . . .	29
3.4	Comparison of morning and evening Quality Control scores. . . . .	30
3.5	Comparison of Quality Control scores by exposure time. . . . .	30
3.6	Demonstration of the QC score cut. . . . .	31
3.7	Difference of Huntsman and Skymapper magnitudes for a collection of stellar sources in a single field. . . . .	32
3.8	Variation in zeropoint determined on a per exposure basis. . . . .	33
3.9	Zeropoint over time, after correction for atmospheric extinction. . . . .	34
4.1	Variation in twilight gradient orientation during the twilight observational window. . . . .	37
4.2	Estimation of twilight gradient from the ratio of morning and evening master flats. . . . .	38
4.3	Linear gradient removal from flat to master ratio images. . . . .	39
4.4	Identification of residual circular features found in G band twilight flats, sorted by local time. . . . .	40

---

4.5	Identification of residual circular features found in R band twilight flats, sorted by local time. . . . .	41
4.6	Comparison of a master night flat to a master twilight flat. . . . .	43
4.7	Galactic cirrus emission identified within a night flat frame. . . . .	44
5.1	A collection of master twilight flats produced for different camera and filter combinations. . . . .	46
A.1	Figure 4.5 sorted by date. . . . .	52
A.2	Figure 4.5 sorted by exposure time. . . . .	53
A.3	Figure 4.5 sorted by CCD temperature. . . . .	54
A.4	Figure 4.5 sorted by cooling percentage. . . . .	55
A.5	Figure 4.5 sorted by date. . . . .	56
A.6	Figure 4.5 sorted by exposure time. . . . .	57
A.7	Figure 4.5 sorted by CCD temperature. . . . .	58
A.8	Figure 4.5 sorted by cooling percentage. . . . .	59

# List of Tables

2.1	Summary of data collection time-line. . . . .	20
-----	---	----



# 1

## Introduction

### 1.1 Background & Significance

#### 1.1.1 Theory

In modern astrophysics Lambda Cold Dark Matter ( $\Lambda$ CDM) is widely accepted as the standard model of big bang cosmology. It successfully describes many of the phenomena that we have observed in the known universe: The Cosmic Microwave Background (CMB), large scale distribution of galaxies and the accelerating expansion of the universe. It is only once we reach the scale of individual galaxies that observations start to show some conflict with theoretical expectations in a  $\Lambda$ CDM universe.

One of the features of  $\Lambda$ CDM is that the universe is almost self similar at all scales, as evident from the primordial spatial power spectrum constructed from CMB data [7]. This observation has direct implications on how the largest structures in the universe should form, how galaxies clusters evolve and should describe individual galaxies and their associated satellite

galaxies [25]. It appears to work on the largest scales, but a large discrepancy emerges between the predicted quantity of satellites and the observed scarcity of them around the Milky Way and other nearby galaxies. This is known as the “missing satellite problem” [17].

The “too big to fail problem” relates to the discrepancy between the predicted number of massive dark matter sub halos around a primary galaxy dark matter halo and the observed number of *massive* satellites. Not only do we not see enough satellites (which are perhaps too small or faint to see), we don’t see enough massive ones (which are much easier to spot). If we match the largest known Milky Way satellites to appropriately sized Dark Matter subhalos from  $\Lambda$ CDM simulations, we are left with an excess of simulated massive Dark Matter sub halos [5]. These subhalos are so large that it should be impossible for them to not produce stars, hence they are “too big to fail”.

The “plane of satellites problem” is the observational peculiarity of known Milky Way satellites seemingly laying within a common orbital plane. Such ordered systems of this nature are thought to be very rare in a  $\Lambda$ CDM universe, which instead predicts more random distribution [7]. Similar situations have potentially been identified for M31 [14] and Centaurus A [27, 28, 38], although, in all cases the limited number of satellites make it difficult to draw broad, statistically-significant conclusions.

### 1.1.2 Need for Low Surface Brightness Imaging

While there is much work on a theoretical side to resolve these problems[8], from an observational perspective the most immediate issue to resolve is the small sample sizes. Indeed, it is entirely possible that we just find ourselves in a statistically abnormal part of the universe. We need a way of probing small scale structure around a larger sample of galaxies. Unfortunately the faint satellites like those around the Milky Way become incredibly hard to detect at distances larger than  $\sim 5$  Mpc. Satellites around the Milky Way, M31 and even Centaurus A have been identified using resolved star counts [39], which is not a feasible way of investigating galaxies at larger distances.

One solution is a specially designed instrument that can find ultra faint unresolved stellar populations. There are many challenges that must be overcome in order to adopt a surface brightness based approach to expanding our statistical sample of galaxies. All sources of systematic error must carefully minimized, characterized and controlled. The key areas of concern for low surface brightness (LSB) imaging are flat-fielding, point spread function (PSF)

characterization, sky background modeling, general quality control to catch subtle data degrading weather effects as well as the procedure for optimal exposure stacking. Fortunately, the literature contains numerous examples of LSB imaging efforts that have addressed with these challenges, producing an excellent starting point for future efforts.

### 1.1.3 Previous Work

The existence of LSB galaxies was first theorized in 1976 by Mike Disney. It was not until 1986 that the first LSB galaxy was discovered using the photographic amplification techniques of David Malin. The discovery of the galaxy, named Malin 1, was reported in Bothun et al. [4]. The vast extent of this LSB spiral galaxy makes it one of the largest spiral galaxies observed – at a diameter of 200kpc, it is roughly 4 times the diameter of the Milky Way.

Malin 1’s discovery was made possible by the photographic plate technology that, at the time, was being superseded by the advent of Charged Coupled Devices (CCD). While the photographic plates held the advantage of being able to cover a much larger field of view (FOV) and at much higher resolutions than a CCD, they lost out to digital devices due to their low Quantum Efficiency’s (QE), decreasing sensitivity with exposure time, nonlinear colour response and inconvenient storage medium. Initially, CCD based instruments resulted in a reduction of large FOV instruments, so despite the increased QE’s and reduced exposure times, these new instruments were less effective at detecting spatially extended LSB galaxies.

With modern large-format CCD, there have been numerous examples of modern LSB-focused observational projects in the literature. In Tal et al. [36] the 1m Small and Medium Research Telescope System (SMARTS) at Cerro Tololo Inter-American observatory was used to produce deep optical broadband observations. The paper makes only very minimal changes in the reduction techniques to address the challenges of LSB imaging. Still, the results of the study highlight the importance of LSB investigations: in a sample of 55 luminous elliptical galaxies (15-50Mpc away), 73% show signatures of tidal disturbances in their stellar bodies.

In a broader sample (1781 galaxies,  $15.5 \text{ mag} < r' < 17 \text{ mag}$ ,  $0.04 < z < 0.2$ ), Atkinson et al. [3] used the 3.6m Canada-France-Hawaii Telescope to produce a catalogue of LSB tidal features identified within their sample. The study determined that approximately 12% of galaxies show clear tidal features, the figure rising to 18% for weaker detections and 26% for marginally identified features. Red galaxies were also found to be twice as likely to

contain tidal features when compared to blue galaxies.

In another body of work, Martínez-Delgado et al. [19, 20, 21] used data from a 0.5m Ritchey-Chretien telescope located at BlackBird Remote Observatory with relatively standard reduction procedure to investigate signs of past accretion events preserved in the halos of nearby galaxies. The observations carried out in Martínez-Delgado et al. [19] and Martínez-Delgado et al. [20] demonstrated that even isolated galaxies can be found to contain LSB accretion fossils (the remains of disrupted satellite galaxies) preserved in their halos. This provided the impetus for a larger survey of 8 isolated spiral galaxies, which was reported in Martínez-Delgado et al. [21]. The authors report a large variety of LSB features highlighted by their observations including: great arc-like structures, enormous stellar debris clouds, giant umbrella-like structures, isolated shells, giant plumes, long stellar streams terminating in a remnant core and other large scale diffuse structures that potentially represent the remains of an ancient satellite that has since been disrupted.

All these LSB imaging efforts demonstrate the wealth of information that can be extracted from the LSB regime of optical astronomy. However, to push further into the LSB regime requires a unique and optimized approach to both data collection and data reduction. In Sandin [32], Sandin [33], the treatment of the PSF and scattered light within the literature is examined. The authors note that these issues are often relegated to the methods section and rarely treated as a significant individual topic. In fact, a key take away point of Sandin [32] (corroborated in Duc et al. [11]) is that previous studies had mistakenly claimed to have detected the presence of galaxy halos, when in fact what was measured was the contribution of the extended point spread function and the galaxy's bright nucleus. Indeed, the colour profile of the PSF (due to higher reflectiveness of red light by the CCD, Sandin [32], Karabal et al. [16]) creates a "red halo effect" that mimics the presence of an old stellar population but is in fact entirely due to internally scattered light. This effect is also noted in observations conducted with the 3.6m Canada-France-Hawaii Telescope in Duc et al. [11]. The authors state that removal of this effect would require modeling of reflections within the telescope and camera via ray tracing.

As an alternative to in-depth modeling of internal reflection of a telescope, some LSB efforts have made physical modifications to their instruments in order to minimize internal scattering. Feldmeier et al. [12, 13] make several adjustments to the 2.1m telescope at Kitt Peak National Observatory. These include the addition of a black cardboard mask over the

detector dewar window and the baffling of problem areas with black cloth. A clever use of pinhole camera images taken with the telescope allowed them to identify the major sources of scattered light within the optical path.

A larger telescope renovation project was carried out on the 0.6m Burrell Schmidt Telescope [23, 24, 31, 35, 40–42]. The telescope was set up with a Newtonian focus, a flat Newtonian mirror and CCD located at the side of the telescope tube. The close tube design plus Newtonian focus allowed for significant reduction in amount of stray light reaching the detector. Changes were also made to the mounting structure to reduce flexure, filter specific anti-reflecting coatings were applied and light absorbing flocking material was installed inside of the telescope tube. The collaboration has since been very productive and led to several LSB optimized data reduction techniques that will be discussed in later sections.

Among modern LSB projects, one of the more unique is the Dragonfly Telephoto array, which has measured the surface brightness profile of the M101 spiral galaxy down to a reported  $32 \text{ mag arcsec}^{-2}$  in the  $g$  band. This approaches the depth of resolved star count studies carried out on galaxies in the Local Group. The key innovation is the use of commercially produced Canon lenses. The purely refracting based system reduces scattered light by allowing for an unobstructed light path, removing the issue of mirror scattering due to mirror roughness and making use of the optical scattering angle of glass, which is less likely to scatter light down the optical path. This in turn produces a PSF that falls off more sharply than typical instruments at large radii [32]. The commercial availability of these lenses also reduces the cost of the system, allowing multiple lenses to be used in tandem for greater total light collecting area.

While it is clear much can be done to optimize for LSB observation from a hardware perspective, there remain systematic sources of error that must be accounted for in the reduction of data. The amount and exact nature of the reduction will depend on the specifics of the instrument used. In general, quality control and flat-fielding error are the primary concern in LSB imaging efforts.

## 1.2 Observational Issues and Quality Control

Common to all astronomical observations is a need to consider external observational factors that unlike internal hardware effects, cannot be controlled. In the case of optical astronomy,

the primary external concerns relate to weather conditions including humidity, high thin cirrus cloud and any other phenomena that impact the seeing of an observation. These external factors necessitate quality control screening, to ensure these factors do not ruin subtle LSB features in the collected data. LSB imaging generally requires long exposures spanning days or even months. Meaning there is a considerable amount of time and data that must be carefully monitored to ensure degraded data can be identified. The time scale over which data degradation can occur is very short, as atmospheric turbulence is highly variable and can noticeably affect seeing on a timescale of minutes [29, 30].

One highly effective metric for quality control is the measure of photometric zeropoint [22, 31, 45]. Testament to its effectiveness, Zhang et al. [45] states that roughly 25% of images rejected in quality control were only identified by zeropoint monitoring. Rudick et al. [31] states that any data on nights where the zeropoint varied by more than  $2\sigma$  of the mean (approximately 0.02 mag) was excluded from their final data set. In Zhang et al. [45], a 0.1 mag deviation from the nominal zeropoint is considered grounds for rejection. Zhang et al. [45] also notes that for Dragonfly, the stellar aureole varies on a timescale of minutes and is likely atmospheric in nature. This differs from other instruments whose wide angle PSF is dominated by internally scattered light. The source for this variation is suggested to be high-atmosphere aerosols such as ice crystals [10].

The effect of airmass (the column of air along the telescope line of sight) is a function of instrument pointing and can be accounted for. However, the instrument pointing itself can be a source of data quality degradation. In Feldmeier et al. [13], the authors discovered large scale flat-fielding errors in some of their data. Upon searching for possible correlations with seeing, lunar phase or time of observation, a relationship with the hour angle of the observations was found. Good data was taken east of zenith, the bad to the west. They concluded that the flexure of the telescope was effecting the flat-fielding of the data. The authors reasoned that rather than create two sets of flats of reduced exposure time, it was better to simply adopt a higher error for the western data. The explicit care taken by the Burrell Schmidt team to ensure the rigidity of their instrument likely has allowed them to avoid this issue [35].

The final major quality control concern for a LSB imaging project exists further afield. Foreground dust contained in the Milky Way (called Galactic Cirrus) can easily mimic the appearance of the LSB emission we wish to investigate. Unfortunately, there is not much we

can do to fix this, other than to observe targets away from the plane of the Milky Way. When analyzing observations we can also refer to infrared observations of the Milky Way, such as those taken by the High Frequency Instrument (HFI) camera (858GHz,  $350\mu\text{m}$  emission) on the Planck telescope [18]. The relatively (to optical) poorer spatial resolution of the HFI camera can make it hard to identify subtle examples of cirrus. Duc et al. [11] note that more subtle patches of cirrus emission can be identified due to the tendency for cirrus to present as parallel bands of emission across an image.

### 1.3 Flat-Fielding

Once the quality of the raw data is assured, the data reduction process can proceed. Flat-fielding is one of the most important steps in LSB imaging: reaching a surface brightness depth of  $30\text{ mag arcsec}^{-2}$  requires flat-fielding errors of less than 0.1% [1]. Conventionally, flat-fielding is carried out using observations of the twilight sky or the uniformly illuminated inside wall of the telescope's dome. Within the literature, several authors have noted that dome flats were not sufficient for their work, due to the difficulty in managing scattered light within the dome [12, 13, 37]. Concerns have also been raised about differences in the colour of the twilight sky and the night sky [12, 13], ruling out the use of twilight flats for some. As a result a majority of LSB flat-fielding seems to have been carried out using night sky flats, constructed from individual dark sky observations or from the actual science frames.

Most flat-fielding schemes have a lot of similarities in their approach. A fairly typical example can be found in the procedure adopted by Feldmeier et al. [12, 13]. To begin the flat frames have overscan removal, bias subtraction and object masking applied. Next they are individually inspected for bright stars and evidence of scattered light patterns. Those that pass inspection are then prescaled by their individual modes and combined into a preliminary flat-field using a  $2\sigma$  pixel rejection. The individual flats are then divided by the preliminary flat and the pixels re-binned into  $50\times 50$  blocks. Planes are then fitted to each frame to deal with sky gradients caused by effects like airglow. The flats are then divided by their normalized fitted planes and the modes of each flat are recalculated and the entire procedure repeated. This cycle continues until the calculated modes numerically converge, which according to Feldmeier et al. [12] takes 15 cycles.

In work done by the Burrell Schmidt collaboration [23, 31, 40], a very similar iterative

flat-fielding procedure is used. Of some interest is the observation that no discernible difference was found in flat-fields constructed from various subsets of night frames (object by object or run by run). The only temporal variation noted was a mild seasonal gradient that was trivial to correct. This allowed for the creation of a single master flat from all flat exposures.

In Watkins et al. [42], the flat-fielding procedure is tweaked to be optimized for narrow band imaging. The modifications were required due to the fact that low counts in narrow band precluded the construction of a master flat from night flats alone. To work around this, a combination of twilight flat and night flat exposures were used (equal night flat exposures to target exposures). All twilight frames were median combined and a night sky flat was produced using the standard procedure described in Watkins et al. [40, 41]. Then, in order to isolate the significant twilight flat gradients, the twilight flat was divided by the night sky flat. The twilight flat gradient could then be modeled and divided out of the twilight flat. The authors claim this was mathematically equivalent to using the night sky flats (except for uncertainty in the gradient models) but with improved Poisson statistics on small scales from the twilight flats.

In Trujillo & Fliri [37] similar arguments are made regarding the insufficiency of dome and twilight flats. Rather than using dedicated night sky flats, the authors instead opt to use the science frames themselves. This is enabled by the unique nature of the authors chosen dither pattern. It is a combination of a fairly standard 9 point dither pattern (one arc-minute offsets) and a position angle (PA) rotation between dither cycles. Each 9 point dither cycle the CCD is rotated by 120 degrees, every three rotations a small rotational offset (10 degrees) is applied. In this manner both the science target and the empty sky regions are sampled over a wide portion of the CCD. This also ensures that internally scattered light effects are not affecting exposures in a consistent manner, making them easier to remove upon median stacking. With some aggressive object masking applied before hand, the science images can be normalized and median combined into a master flat for each night of observation.

Among those who choose to use twilight flats instead, the primary challenge is the correction of the gradient in the twilight sky. A comprehensive analysis of twilight sky gradients was made by Chromey & Hasselbacher [9]. In their investigation, the magnitude of the twilight gradient was measured at a number of altitudes, azimuths and apparent zenith angles of

the sun (the distance below the horizon). A key finding of their work is the stability of twilight gradients over the period for which the sun is less than 10 degrees below the horizon. It is also stated that gradients are directed along lines of constant azimuth and that a null point exists close to zenith but offset 0 to 40 degrees toward the anti-solar horizon. Within this region gradients of less than 1% per degree are reported. A similar result is measured by Wei et al. [43], who measure a 1% gradient over their  $1.47 \times 2.93$  FOV.

Even with special care given to flat-fielding, reflecting based instruments typically only reach a surface brightness depth of 28 mag arcsec<sup>-2</sup> [2, 19–21]. With careful considerations of LSB imaging requirements, the Burrell Schmidt collaboration has reached 29 mag arcsec<sup>-2</sup> when imaging the centre of the Virgo cluster. In the case of Dragonfly, Abraham & van Dokkum [1] claim the lenses used are optimized for excellent field flatness. Furthermore, the multiple apertures in the array also compensate for any small flat-fielding errors or scattered light effects. This is due to the fact that these effects will present differently in each individual lens, so upon image combination a lot of these errors will be smoothed out. According to Merritt et al. [22], after an initial dark subtraction and flat-fielding, all that was required was a simple second order polynomial fit and subtraction to a residual background gradient (due to changing sky background with zenith distance). The flatness of the images is attributed to the large dithers and stability of the instrument [1, 22].

## 1.4 Structure of Thesis

In this thesis I examine the important process of flat fielding, as it pertains to Low Surface Brightness imaging and Huntsman Telescope data specifically. The structure of the thesis is as follows. In Chapter 2, I give a basic overview of the Huntsman data that will be discussed. This includes the observing process for collecting the data, the basic data reduction steps required for processing the data, the time line and quantity of data collection and the known sources of data degradation. In Chapter 3, I outline possible flat field methodologies that may be adopted for Huntsman, including the data quality control procedures that could be used alongside them. In Chapter 4, I carry out these methodologies and finally in Chapter 5 I discuss the outcomes of the work in Chapter 4 and discuss the implications for the operation of the Huntsman Telephoto Array.



# 2

## Methods

The Huntsman Telescope will eventually be run as an entirely automated instrument. However, over the course of this thesis the telescope has operated with varying levels of manual input and automation. Naturally, this has resulted in numerous bugs and human errors that have had an impact on the quality of data collected. While this is somewhat undesirable for any immediate science goals, it does provide a useful data set on which to test some coarse quality control measures. In this Chapter I will discuss the main analysis and data preparation methods employed within this thesis. I will discuss how and when Huntsman data has been collected during the course of this thesis, including how these methods have changes as the system has been developed and improved by other members of the huntsman team. Next I will provide an overview of how huntsman data is reduced followed by an overview of the time line of data collection and description of known sources of obvious data degradation. Finally I will give an overview of the masking routine utilised for flat-field processing as well as a description of a the primary data production used regularly through out this thesis.

## 2.1 Observing with the Huntsman Telescope

The Huntsman Telescope is seated on a Software Bisque Paramount MEII<sup>1</sup> robotic telescope mount at the Huntsman Observatory within Siding Spring Observatory. The operation of the mount and observatory dome are controlled by a piece the proprietary software, TheSkyX Professional<sup>2</sup> from Software Bisque. The control of the Huntsman Telescope hardware (cameras and lenses etc) is controlled by software that has been developed for Project PANOPTES<sup>3</sup>, called the PANOPTES Observatory Control System or POCS. It is an open source modular Python 3 library based on a state machine architecture, with a specific design emphasis on flexibility and customization. This made it an ideal choice for Huntsman and its' specific hardware requirements, the Huntsman specific modifications to POCS is available here<sup>4</sup>.

POCS is designed to be initialized only once to be then left running at all times. The system will automatically put the telescope and dome into a sleeping state during the day. It will then automatically resume observations in the evening if POCS determines the weather is safe for observing. The first observational run carried out as part of this thesis was undertaken from the 5<sup>th</sup> until the 10<sup>th</sup> of February 2018. At this point in time, the mount and telescope could be controlled via POCS but only in a mode with three lenses (ultimately Huntsman will have 10) controlled by one control computer<sup>5</sup>.

During this period of time a typical night of observing would begin 30-45 minutes before twilight. All required hardware was assessed and power-cycled if necessary and then TheSkyX was initialized. Finally POCS was initialized, proceeding to enter its day time sleep mode as usually was before sunset. Upon reaching twilight, POCS initiates a twilight flat procedure that slews the telescope from park position to a predetermined twilight flat pointing positioned roughly opposite from the setting sun. During the February 2018 run, the dome had to be manually rotated by someone physically at the dome. A consequence of the need for manual rotation was occasional dome vignetting, either due to cameras exposing before the dome had time to rotate or simple dome misalignment due to human error.

---

<sup>1</sup><http://www.bisque.com/sc/pages/ParamountMEII.aspx>

<sup>2</sup><http://www.bisque.com/sc/pages/TheSkyX-Professional-Edition.aspx>

<sup>3</sup><https://projectpanoptes.org/>

<sup>4</sup><https://github.com/AstroHuntsman/huntsman-pocs>

<sup>5</sup>While the USB protocol in theory allows computers to have up to 128 USB devices, we discovered in practice modern computers can only have a limited number of USB drivers.

After the twilight flat sequence completes, POCS then waits for the sun to descend below an elevation of -18 degrees from the horizon. At this point in time POCS determines an optimal target from a prioritized target list and directs the mount to slew to the required coordinates. If by morning observations had not already been abandoned for weather concerns, a second round of morning twilight flats were obtained by POCS.

The twilight flat exposure times were set to achieve target mean ADU of 10,000 (after dark subtraction), with a minimum acceptable mean of 5,000 ADU and a maximum acceptable mean of 15,000 ADU. To achieve a roughly constant count rate, we used a model utilised by the Dragonfly team to predict the exposure time of the next flat image given the current sky background levels of the data just obtained:

$$t_{exp} = t_{prev} \left( \frac{ADU_{target}}{ADU_{prev}} \right) \left( 2^{\frac{t_{elapsed}}{180}} \right) + 0.5 \quad (2.1)$$

Here the exposure time for the next flat-field exposure ( $t_{exp}$ ) is determined from the exposure time of the previous flat-field ( $t_{prev}$ ), the ratio of the target mean ADU and the mean ADU of the previous exposure ( $ADU_{target}$  and  $ADU_{prev}$ ) and the total elapsed time of the current twilight flat-field sequence ( $t_{elapsed}$ ). As evident in Figure 2.1, this method produces a fairly homogeneous set of flat-field exposures within the desired mean ADU range. It is also clear that over a given twilight sequence we can expect to produce 10-20 exposures before the illumination provided by the twilight sky becomes insufficient.

Two additional observation runs were made during the time line of this thesis. The second occurred from the 14<sup>th</sup> to the 25<sup>th</sup> of May 2018. Fortunately by this time, the issues relating to the syncing of the dome and telescope movements had been largely resolved. The operating procedures was the same and human supervision was still required as the dome shutter was not remotely controllable. Dome vignetting still occurred intermittently, at times interfering with Huntsman's auto focus routine. It was determined that this would occur only for pointings directed close to overhead. Further tweaking of the dome geometry parameters in TheSkyX greatly reduced the occurrence of this issue over the run, although occasional slight dome vignetting still occurs intermittently while pointing at certain directions in the sky.

The final major observational run (for which the author was only assisting remotely) occurred from the 23<sup>rd</sup> to the 27<sup>th</sup> of July 2018. During this period of time Huntsman was

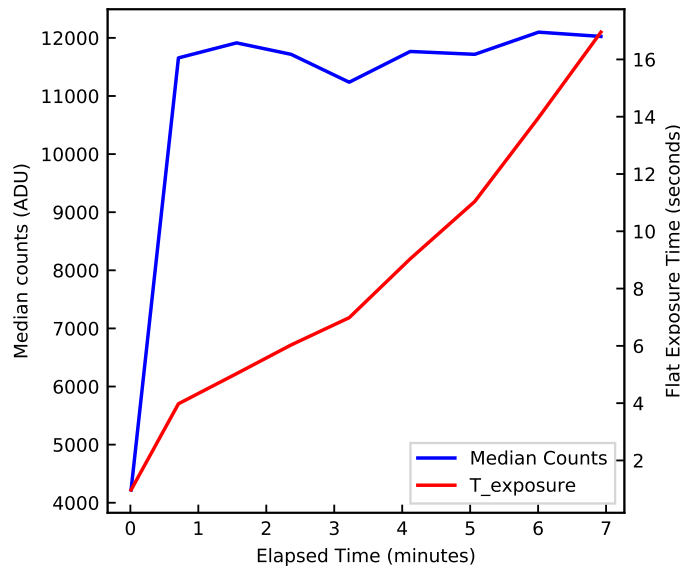


Figure 2.1: Red line and right y-axis shows exposure times for a typical evening twilight flat-field observing sequence. The exposure time is adjusted in real time according to Equation 2.1 in order to deliver a consistent median count level in each exposure (blue line, left y-axis).

transitioned from running on a single central computer (capable of running only three cameras at a time) to a mode where each camera was operated by an individual Raspberry Pi, which in turn communicates with a central control computer. This had the benefit of allowing more than three cameras to be in use at any given time, as well as to allow each camera to be individually power-cycled if required. Previously, the entire system would have to be reinitialized in the event that one of the cameras hanged upon exposure readout. At this point, Huntsman could be run in a mostly hands off manner, only requiring human intervention in the event of bad weather and to close the shutter at the end of the night.

The data collected from these three observation runs are what is used for the bulk of this thesis. As of mid September 2018, Huntsman has been capable of remote observing due to the addition of a functional remote switch for the dome shutter and the resolution of some network access restrictions. However, as the weather monitoring system and shutter controls have not been adequately stress tested, Huntsman has still only been operated infrequently and only recently was run when on-site assistance was not available.

## 2.2 Preparation of Master Darks

Dark frames are exposures taken with a closed shutter, such that the only signal recorded is due to thermal current flowing and the bias voltage applied to the CCD. The dark current increases with temperature and will scale linearly with exposure time. For Huntsman, we aim to build up a library of master darks<sup>6</sup> for varying exposure times and CCD temperatures by stacking many individual dark frames of set temperature and exposure time, as shown in Figure 2.2.

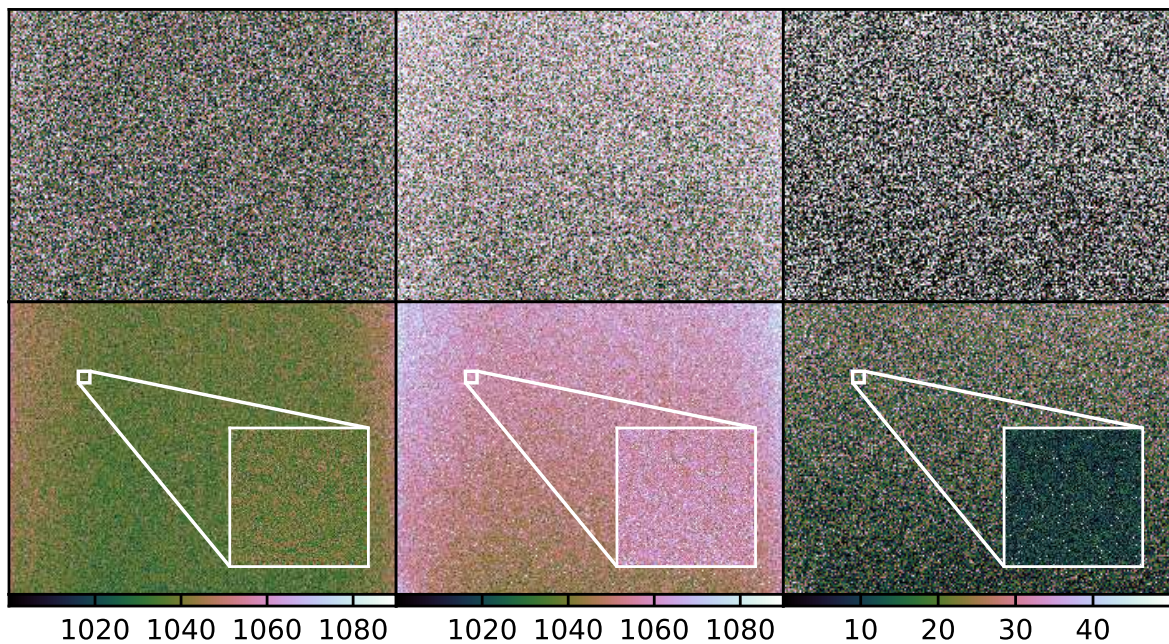


Figure 2.2: From left to right, each column shows a zero second dark 0°C (bias), a five minute dark 0°C and the difference of the two. Top and Bottom rows compare single exposure and 19 exposure median stack versions of the same data products. Colour-bars illustrate the count levels in Analogue to Digital Units (ADU) for each column of panels.

The dark current signal (and included bias signal) needs to be subtracted from all other forms of raw data, which includes both flatfield data and science data. For science data, the procedure is straight forward: simply select a master dark of matching exposure time and CCD temperature and subtract it from the raw science frame. For most of these fairly standard CCD data processing tasks (such as dark subtraction) we make use of the python package CCDProc<sup>7</sup>, which carries out the error propagation and unit checks for the user.

<sup>6</sup>A master dark is the name given to a median stack of a large number of equal exposure time and CCD temperature darks.

<sup>7</sup><https://ccdproc.readthedocs.io/en/latest/>

## 2.3 Preparation of Flat-Field Data

In astronomy, a flat-field is a form of calibration used to correct imperfect illumination of a detector, as well as to correct for variations in sensitivity between detector pixels. The idea is simple in theory: produce an uniform source of illumination and make an observation. Any deviation from homogeneity in the resulting data (once several such observations have been stacked to minimize noise) can then be used to appropriately scale each individual pixel in further observations.

### 2.3.1 Twilight Flat-Data Preparation

In the case of twilight flats, the exposure times can vary from a few seconds to up to a minute, so it is more convenient to take specific darks to match the various flat exposures in a given twilight sequence. Once individual twilight flats have been dark subtracted they require masking before median stacking. This is more important for longer exposures (e.g. when the twilight sky is dimmer) as stars begin to appear in the flat-field images. An additional complication to this issue is that it is not possible to focus the lenses before twilight, meaning these stars may be slightly out of focus. This makes them harder to separate out from the smooth background of the twilight sky.

In order to mask stars in the twilight data, the CCDProc `median_filter` function is used (with a kernel of  $11 \times 11$  pixels) to create a model of the smooth sky background of the twilight. This background map is then subtracted from the flat, leaving the excess signal from the stars. The `make_source_mask` function from the `photutils` [6] python package is then used to create a mask for regions affected by any stars. By using aggressive masking threshold and dilating the resulting source mask, we can attempt to minimise the amount of starlight that contaminates the master flats. After the masking, the individual twilight flats are normalized according to the median value within the central region of the flat frame. Finally they are median combined using the CCDProc `combine` function.

### 2.3.2 Night Flat-Data Preparation

For twilight flats, the number of sources to mask is relatively low making it more feasible to catch all the undesired signal by using very aggressive masking and mask dilation. When masking a typical night frame for the purpose of creating a night flat, there must be a balance

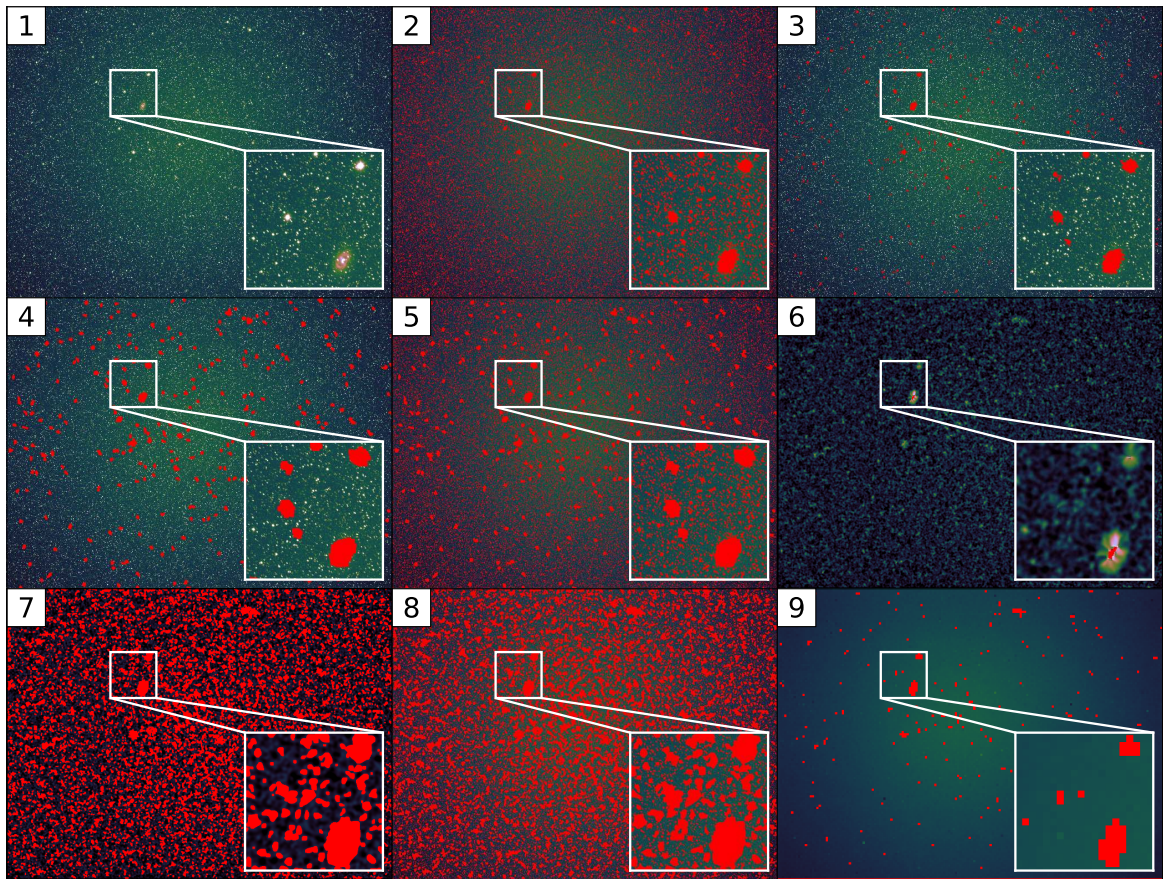


Figure 2.3: The various steps in the adopted source masking procedure, a description of steps taken within each chronologically numbered panel is given within Section 2.3.2.

Masked pixels are displayed as a solid red.

between masking aggressively enough to remove all unwanted signal but not to the point where we needlessly discard large amounts of useful data.

Initial attempts to use the same twilight data masking method for the night flats purposes proved problematic: after source masks are aggressively dilated, almost every pixel in the field of view is masked. An alternative approach was therefore developed, which is shown in Figure 2.3 and is outlined here:

Step (1) We start with a dark subtracted night frame.

Step (2) A smooth background component is modeled and subtracted using the `CCDProc median_filter` function, and a  $3\sigma$  source mask is then produced using the `make_source_mask` function from `photutils`. This mask is then processed using the `scipy.ndimage binary_closing`[15] function to round the source masks and fill in any small regions enclosed by masked pixels.

- Step (3) A second round of source detection is run on the mask produced in Step (2), with parameters set to only identify sources consisting of more than 300 connected pixels (ie a circular region of radius  $\sim 10$  pixels). This second mask identifies large objects such as bright stars and galaxies within the frame.
- Step (4) The large object mask is again processed `scipy.ndimage binary_closing` function and then dilated using a the `scipy.ndimage binary_dilation` function and a  $11 \times 11$  pixel kernel.
- Step (5) The masks generated in Step 2) and Step 4) are combined into one.
- Step (6) Using the mask from Step 5), the original image is masked and then convolved with a Gaussian kernel to interpolate over the masked values.
- Step (7) A final round of source detection is run on this interpolated image to identify regions of faint signal missed in previous rounds of source detection.
- Step (8) The final mask is created as the union of the masks created in Step 2), Step 4) and Step 7).
- Step (9) For illustration purposes, the original night frame has been masked using the mask created in Step 8). This masked image has then been  $50 \times 50$  pixel median binned, revealing a smoothly varying background produced by the combination of night sky illumination and the Huntsman vignetting pattern.

Once enough masked night frames have been produced, they can be combined into a master night flat in a similar manner to the twilight flats. With the master flat (night or twilight) created, it can be used to correct the dark subtracted science data for the inconsistent illumination pattern produced by the optics. This includes the large scale vignetting pattern, as well as pixel to pixel variations in sensitive that are unique to each CCD.

## 2.4 Data Collection & Data Degradation

As outlined in Section 2.1, the data utilised in this thesis was collected over three on site observing runs. During these periods, the telescope had varying levels of automated control, which resulted in some intermittent data degrading effects, some of which are display in

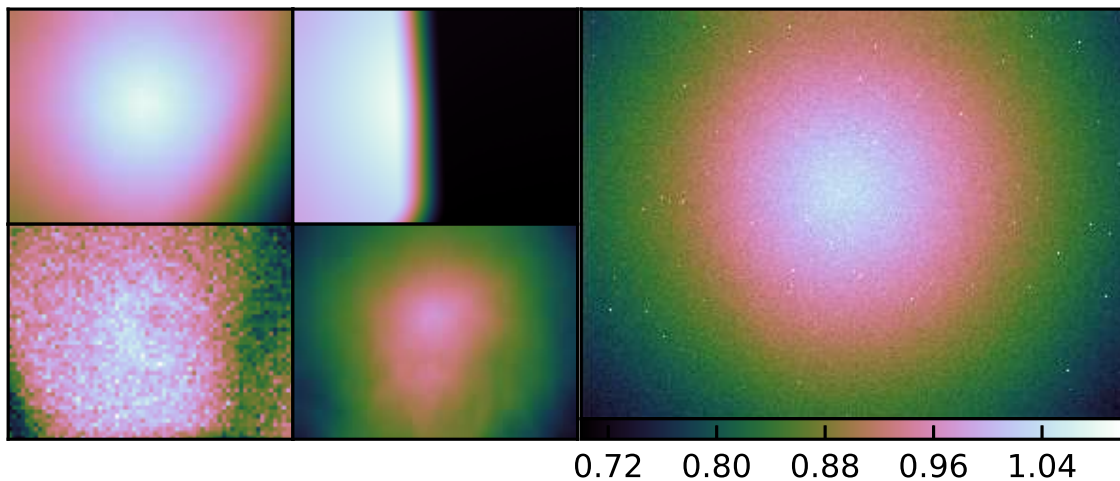


Figure 2.4: Examples of bad quality data shown in the left hand  $2 \times 2$  panel, from the top left panel going clockwise; dome vignetting, intermittent shutter clearing error, clouds and short exposure time shutter gradient (displayed as binned ratio with a master reference flat). The right panel displays an example of a good quality, unmasked G band morning flat. From this it can be noticed that the Huntsman flat-field is dominated by a vignetting pattern that attenuates a uniform illuminate by up to 30% at the peripheries of the CCD.

Figure 2.4. The most obvious of data quality issues was when there was a misalignment of the dome and the telescope due to human error or poorly configured dome geometry in the mount control software.

Two other subtler sources of data degradation resulting from a physical obstruction were also detected during the analysis stage of this thesis. The first is an infrequent error that results in a camera shutter failing to clear during an exposure. It is unclear at this time what the cause of this hardware malfunction is, but from a practical point of view it can be screened for using whatever method is deemed appropriate for dome vignetting.

The second subtle issue also pertains to the camera shutter. It is apparent only in very short ( $< 1$  s) exposures, such as those taken for twilight flats. As can be seen in Figure 2.4, short exposures seem to exhibit a noticeable gradient along the long axis of the CCD, indicating it is likely an affect tied to the rolling nature of the shutter mechanism. This issue is easily rectified by requiring a minimum exposure time for twilight flats and science data. Another considerable and mostly obvious source of data degradation is overcast weather. As Huntsman is not yet collecting live weather data, additional methods are needed to screen for data impacted by clouds.

Date	83F010774			83F011167			83F010639			83F011791		
15/05/2018	9	9	0	9	9	2	–	–	–	9	9	4
16/05/2018	16	13	0	16	13	5	–	–	–	16	14	6
17/05/2018	9	8	0	–	–	–	–	–	–	9	8	0
18/05/2018	12	12	0	–	–	–	–	–	–	12	11	2
19/05/2018	9	8	8	9	8	8	–	–	–	9	8	0
20/05/2018	9	9	8	9	9	7	–	–	–	9	9	8
21/05/2018	15	13	3	15	13	3	–	–	–	15	13	3
21/05/2018	9	8	0	9	8	0	–	–	–	9	8	0
22/05/2018	9	8	8	–	–	–	9	8	8	–	–	–
23/05/2018	16	14	4	–	–	–	16	15	5	–	–	–
23/05/2018	9	8	8	–	–	–	9	8	8	9	8	8
24/05/2018	15	14	0	–	–	–	15	14	0	15	13	1
11/06/2018	9	9	0	–	–	–	9	9	0	9	9	0
1/08/2018	9	8	0	–	–	–	–	–	–	–	–	–
1/08/2018	9	8	0	–	–	–	–	–	–	–	–	–
2/08/2018	17	13	3	–	–	–	17	13	3	–	–	–

Table 2.1: Flat-field data collection time-line for the four active cameras on Huntsman (83F010774, 83F011167, 83F010639 and 83F011791). For each Camera and Date entry, three numbers are recorded: number of flat exposures taken, number that have approximately the target sky levels and number of good quality flats. Entries marked with – indicates the camera was not used on that date

The common feature of most of these data degrading effects is that they only appear intermittently or vary rapidly on timescales approximately equal to the exposure time of a single image. For example, the position of a vignetting dome in a cameras Field of View will be constantly changing as the dome rotates to track the target and the telescope itself moves through its dither pattern. Also clouds move and distort noticeably during an exposure and between subsequent images.

This time-varying component is a useful feature that we can exploit to screen flat data for these degrading effects. As outlined in detail further below, the automated screening method involves taking a set of twilight flats from an evening, processing them all and producing

an initial dirty master flat (dirty in the sense that no effort has been made yet to identify bad quality data). The individual flats can then all be assessed relative to the dirty master flat according to some metric and iteratively kept or discarded and reevaluated compared to a new dirt master flat, until either the deviations converge to predetermined level or none of the flats are found to be similar to one another. The key to this method is the fact that good flat-fields are very alike and even exposures vignettted by a stationary dome show significant variation over short timescales. A more in depth discussion of twilight flat screen methods will be giving in Section 1.2. After a screening method such as the one described in Section 1.2 is employed, much of the collected data is deemed unusable as shown in Table 2.1. It is however encouraging to see that the poor quality data can be identified in an automated fashion.

## 2.5 Quality Control Diagnostic

In this section, I describe the main diagnostic measures to determine whether a flat is of good quality or not. This includes a diagnostic image for illustration purposes and a single quantity, which relates the expected variation of a flat above the expected level from a good-quality flat image.

Throughout much of this thesis I will be assessing the quality of individual flat exposures (Night or Twilight) repeatedly. To do so requires reference to some form of standard for a good quality flat. As a result I most often show the ratio of an individual flat to some normalised reference master flat, as opposed to simple showing just the flat itself. I will refer to these data products as “*flat to master ratios*” as defined in Section 2.2, where each pixel value indicates the ratio of the pixel value in the normalised individual flat with the corresponding pixel value in the reference master flat.

$$flat\ to\ master\ ratio = \frac{flat_{individual}}{flat_{master}} \quad (2.2)$$

In the case where the reference master flat is produced from a single set of twilight observations, any frames affected by data degradation will show noticeable deviation in their flat to master ratio. This can allow for iterative rejection of bad flats through repeated comparison to reference master constructed from all the flats remaining in a sequence. Once only good flats remain, the flat to master ratios will have converged to one another. Even in the

scenario where an entire sequence is impacted, the variations produced by things such as cloud or dome vignetting change on short timescales, meaning the flat to master ratio will not converge to a predictable limit, or any limit at all.

Any deviation between *good quality* flats should converge to a predictable value when they are co-added. The predictable limit that the flat to master ratios of a good set of flats will converge to is dominated by Poisson noise (readnoise for the cameras is only  $9.3 e^-$ ). More explicitly, the standard deviation in the value of a given pixel between a set of good quality flats should be described by Equation 2.3:

$$\sigma_{Poisson} = \sqrt{N} \quad (2.3)$$

In Equation 2.3  $N$  is the number of events being counted and the resulting Poisson noise is the statistical uncertainty in the number of events counted.

In our case, we are counting electrons collected in a CCD pixel, which is recorded as analog to digital units (ADU). Given the gain in Huntsman CCDs is approximately 0.36 electrons per ADU, we can determine an expected Poisson noise error in our flats by considering our target ADU count level (Equation 2.1) and the number of counted electrons that represents. The expected Poisson noise error in ADU is given in Equation 2.4

$$\sigma_{Poisson}^{ADU} = \sqrt{Gain \times N_{ADU}} \quad (2.4)$$

So for typical twilight flats, the targeted mean count level is 10,000 ADU, which corresponds to a fractional uncertainty due to just Poisson noise of 1.7%. As shown in Figure 2.4 there is a roughly 30% decrease in intensity towards the peripheries of the CCD due to vignetting by the optics. The expected fractional uncertainty due to Poisson uncertainty at the edges of the field of view will thus increase slightly to 2.0%.

In the following Chapter, I will explore the use of the standard deviation of the flat-to-master ratio frames and any deviations from the expected Poisson noise levels for a good flat (1.7 – 2.0%) as a tool for assessing the quality of individual flats. For the remainder of the thesis I will refer to the standard deviation of the flat to master ratio frame as the “quality control score” (QC score).

# 3

## Flat-Fielding Expectations, Strategy and Quality Control

### 3.1 Theory and Expectations

The key innovation for Huntsman's potential as instrument optimised for Low Surface Brightness imaging are the unobstructed optical paths of its refracting lenses. The lack scattering surfaces between the incoming light and the CCD allows Huntsman reduces systematic uncertainties from scattered light reach a lower surface brightness limits. This does not mean Huntsman is free of such issues, as the surface brightness floor is pushed lower, new sources of error become significant. A major source of systematic error is likely to be flat fielding as illustrated in Figure 3.1. Simple propagation of flatfielding uncertainties indicates they need to be smaller than 0.1% to reach interesting surface brightness levels of  $\sim 30 \text{ mag arcsec}^{-2}$ .

In this context, there are some factors and trade offs to consider when deciding on the most optimal flat-fielding method for Huntsman. Ideally the source of illumination for a

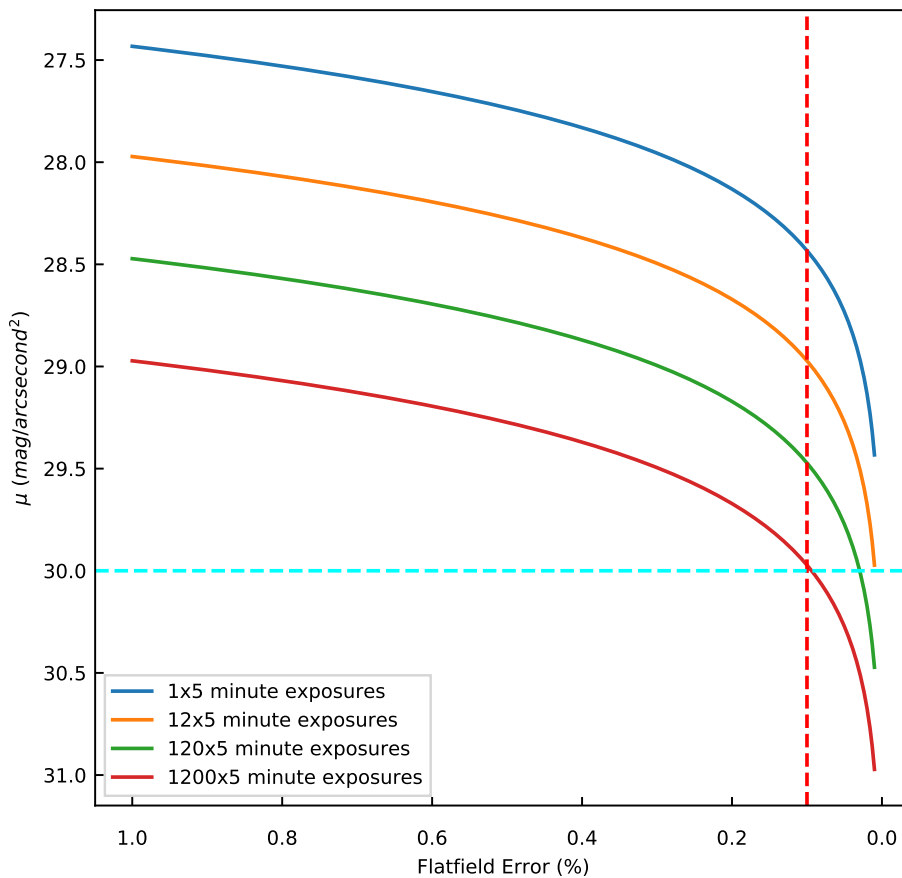


Figure 3.1: The maximum achievable surface brightness depth limit when observations are limited by flat-fielding errors given on the X-axis. The curves show the number of different co-added individual 5 minute exposures, the blue and red dashed lines mark the 30  $\text{mag arcsec}^{-2}$  and 0.1% levels respectively.

flat-field needs to be perfectly flat and have the same spectral energy distribution (SED) to the science targets. Another consideration is the need for individual flat-fields for individual lens and camera pairings. Flat-fields will also need to be refreshed on a regular basis, as dust settles on the lenses over time.

Bearing these considerations in mind, there are three possible flat-fielding modes that are possible for Huntsman: dome flats, night flats and twilight flats. Each method comes with their own challenges, advantages and disadvantages. In the following sections I will describe each method and their suitability for Huntsman.

### 3.1.1 Dome Flats

The dome flat method involves creating an artificial source of illumination within the dome enclosure for the purpose of flat-fielding. The most obvious benefit of such an approach is that it is entirely unaffected by weather. This allows Huntsman to make more efficient use of its time during unsafe observing conditions. Unfortunately, the Huntsman dome is relatively small and made of fiber glass that is somewhat transparent to sunlight. This means that flats could not be taken during the day as stray light from outside would contaminate the flat-field source. The small enclosure of the dome also makes it difficult to control scattered light from the flat-field.

Another draw back to the dome flat method is the difficulty of emulating the SED of the science targets. This is important as the sensitivity of a CDD varies with wavelength, a flat-field constructed from one SED will not accurately correct a science exposure of a different SED source. For this reason, dome flats would require a special light source and special material to construct the illumination screen such that the SED of reflected light is preserved. At this stage Huntsman has not been equipped with these facilities, so an empirical assessment of this method can not be made. The outcome of tests of the other two methods will inform if dome flats should be pursued further.

### 3.1.2 Night Flats

The main benefit of the night flat method is that the SED of the night is a relatively close match to an astronomical source, such as a galaxy. The trade-off is that the night sky is very faint, which means it will take many exposures to build up a master night flat with satisfactory noise properties. This issue is compounded by the presence of stars and galaxies, which need to be aggressively masked in order to isolate the flat night sky component. Dithering of observations (or even multiple pointings) is an important part of this because it ensures that each pixel of the CCD samples a uncontaminated portion of night sky.

To save observing time, the night flats can be created out of scheduled science exposures which are typically going to be located far from the galactic plane to avoid galactic cirrus. This will mean the observed fields will generally be less crowded, require less masking and therefore contain more empty sky.

An additional processing step will also be required for night flats, due to the potential

presence of air glow gradients [26]. These gradients will vary in intensity and orientation over the course of the night. It is possible that these gradients can be modelled and removed as tilted planes in an iterative fashion as in Feldmeier et al. [12] and Mihos et al. [23] or as simple one fit correction [9, 31]. However, the large degree of vignetting in Huntsman optics may complicate these solutions in practice.

### 3.1.3 Twilight Flats

The twilight flat method is perhaps the most popular and convenient form of flat-field, although not generally among other LSB specific efforts [e.g. 12, 13, 23, 31, 37, 40]. As the name implies, the method utilizes the twilight sky as its flat illumination source. While not as close a match to the SED of a galaxy, it still outperforms dome flats taken with standard light sources [12, 13, 37]. The twilight sky is also significantly brighter than the night sky, meaning it is far easier to collect enough photons to produce a master flat with acceptable noise properties.

The drawbacks to this method relate to weather and time frame. Like night flats, twilight flats require perfectly clear skies. Clouds cannot be masked and faint thin clouds can be hard to detect. Twilight flats need to be carefully inspected before being incorporated into a master calibration file and this likely will be done on an automated basis for Huntsman. Twilight flats can only be collected in a short span of time in the evenings and mornings when the sky produces the optimal count levels for a reasonable exposure time.

Twilight flats will also contain gradients since the twilight sky is not perfectly flat and the relatively large field of view of Huntsman. As reported by Chromey & Hasselbacher [9], these gradients are stable until late twilight and can be minimised by pointing towards a null point close to zenith, offset towards the anti-solar horizon. As these gradients will be aligned with the position of the rising or setting sun it may therefore be possible to combine a set of morning and evening flats in order to remove the twilight gradient. This solution will only work if both evening or morning flats are acquired in a given session. Without a set of both, it is much harder to remove the gradient due to the asymmetric vignetting pattern produced by the lenses as shown in Figure 3.2. This may be less of an issue for night flats, if the orientation of the gradients are sufficiently random. This could provide a useful avenue to isolate twilight gradients if only one of the morning or evening twilights are obtained in a night.

## 3.2 Flatfield Data Quality Control

In Section 2.4, several forms of flat field data degradation were discussed. These included degradation due to internal faults such as camera shutter failures or dome vignetting, as well as external effects such as weather. These issues are equally significant for twilight and night flats. However, the differences between the two methods mean that unique approaches to the task of quality control are required. When discussing twilight and night flats in this section, it should be assumed that it is the dark subtracted, masked and normalized form as discussed in Section 2.2. Both night and twilight flats are normalized relative to the median count level of a box scaled to be 30% of the CCD dimensions in size).

### 3.2.1 Twilight Flat Quality Control

In order to understand how we might screen for quality in twilight flats, it is helpful to frame the question in terms of what makes a quality twilight flat. Ultimately we want an observation that is as close as we can get to representing just the response of the lens and CCD to a perfect flat source of illumination. For a good quality flat, the statistical error associated with each pixel should be dominated by the Poisson noise, which as described in Section 2.5 is proportional to the ADU count in each pixel. To facilitate the following analysis, a set of reference master flats with low statistical noise were created with a manual screening and processing. These are presented in Figure 3.2.

The twilight flat observations have been designed so that mean ADU level across the centre of the CCD is approximately 10,000 ADU. The full well capacity capacity of the Huntsman CCDs is 65,536 ADU and initial estimates put the extent of the linear regime as up to at least 60,000 ADU<sup>1</sup>. The relatively low target ADU level for twilight flats was initially set in order to be conservatively within the linear range of the CCD and will likely be increased in the future.

In Section 2.5, I showed that the fractional Poisson noise in a flat with a mean ADU level of 10,000 would range from 1.7% to 2.0% across the highly vignetted field of view. Anything that has a higher noise property compared to expectations from pure Poisson is likely bad.

In Figure 3.3, the distribution of flats (across all cameras and filters) with QC scores less

---

<sup>1</sup>Verification of the linear range of the Huntsman CCDs was not carried out by the author of this thesis.

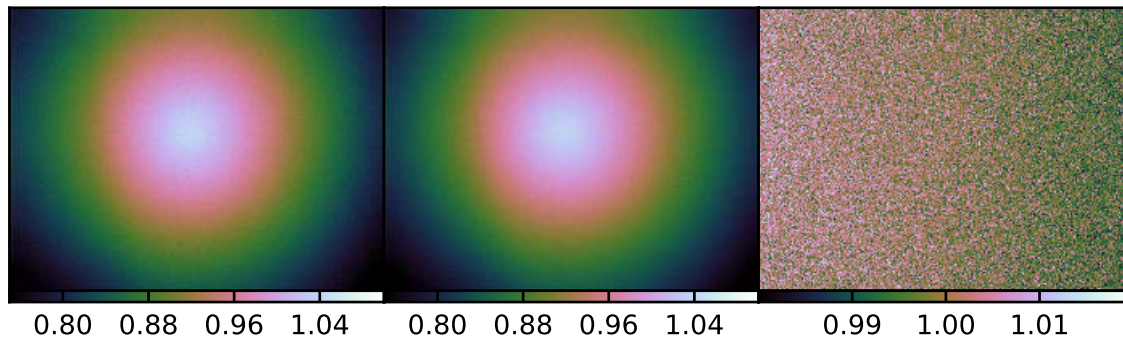


Figure 3.2: For Camera 83F010774 with G band filter, from left to right: (1) reference morning flat master, (2) reference evening flat master and (3) ratio of the morning to evening masters.

than 0.05 is displayed. Immediately apparent in the figure is a large cluster within the 0.01 to 0.02 range. This aligns with the predicted range from Poisson-dominated noise properties for the bulk of the flat field data (see Section 2.5).

A transition at QC Score at  $\sim 0.02$  is also reflected in the selection of morning data taken from a single camera and filter combination is displayed in Figure 3.6, where the panels have been sorted by the QC metric. Given the observations appear to support the expectations from noise properties, in the analysis of Chapter 4. I adopt a scheme where the Quality Control (QC) score (standard deviation of the flat to master ratio as described in Section 2.5) is greater than 2% it is indicative that the data has been degraded in some manner and is discarded.

There appears to be evidence of bimodality in Figure 3.3, which is most apparent for the G band flats but is also present for the R band. While part of this is due to a range of flat backgrounds levels (10,000 is only the average), as can be seen in Figure 3.4, the split in the distribution of QC scores for both G and R band flats seems to correspond to a whether a flat was produced in the morning or the evening.

One possibility for this bimodality might be that we observe a similar effect to the one reported in Feldmeier et al. [13], where flexure of their telescope as it moved between east and west of zenith induced large scale flat field errors in their data. As Huntsman is set to exactly mirror its morning flat position with its twilight position, it may be the distribution of weight on the mount is such that the twilight position places the array under greater strain. While this is an idea that needs to be explored further, I note that the Canon lenses have been

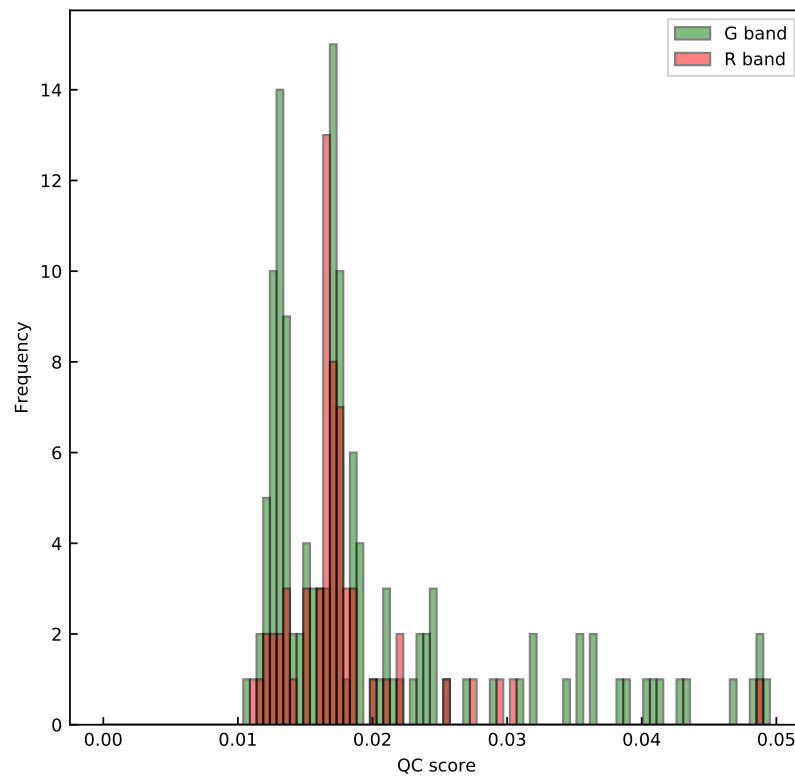


Figure 3.3: Distribution of Quality Control (QC) scores across all cameras, colour coded by the filter used for the twilight flat observations.

secured at both ends with a rigid aluminum tube to minimise flexure.

The QC score is compared to the exposure time of the twilight flat in Figure 3.5. It is clear there is a considerably larger quantity of short exposure, poor quality flats<sup>2</sup>, though it does not appear to cause the bimodality. One possibility is that the telescope was not focused before the evening twilight flatfield images were taken. As result, it is possible that the light from faint and defocused stars that are hard to mask are contaminating the evening flats, resulting in the observed elevation in QC scores. More investigations are needed to determine the source of this bimodality.

<sup>2</sup>The excess of short exposure flats in the evening is a consequence of how POCS operates. Once POCS determines it is close enough to twilight, it will begin taking intermittent 1 second exposures. This process is continued until the flat exposures stop saturating, at which point the exposure time begins dynamically updating to generate flats of at the desired mean ADU level until 10 flats with good background levels are obtained. POCS then continues exposing until a set number of flats have been produced, or the sky becomes too dark. The situation is reversed for morning flats, with exposure times starting high and steadily decreasing as the sky brightens until 10 flats with good background levels are obtained. Thus the excess of short exposure evening flats is a consequence of the sky starting bright and becoming dimmer.

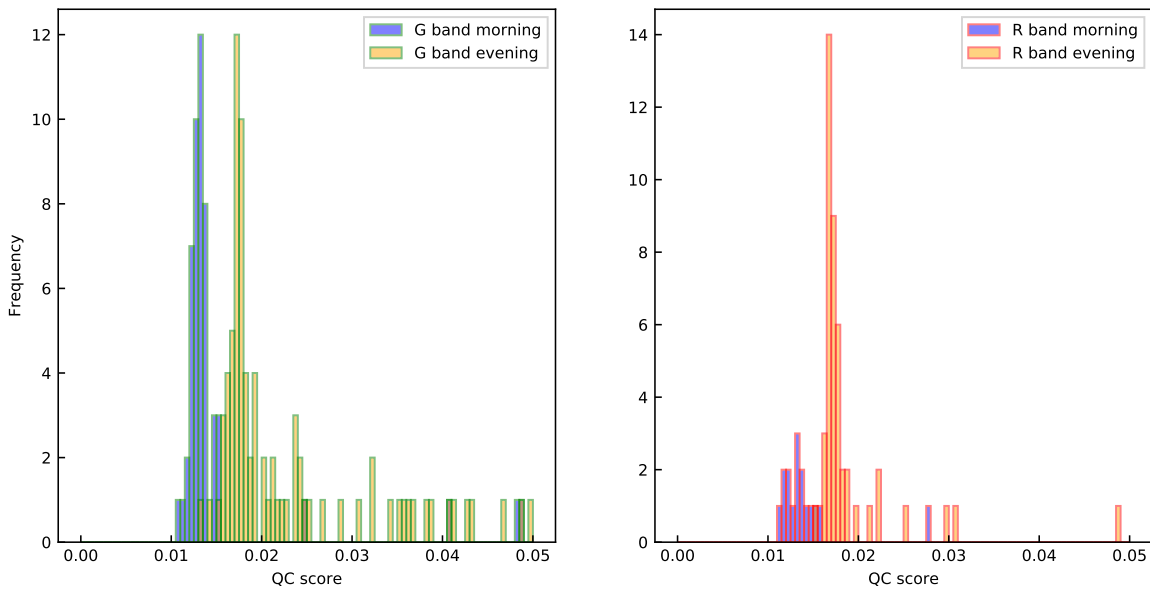


Figure 3.4: Distribution of Quality Control (QC) scores for twilight flats split across two panels based on whether the flat observation was made in the morning or evening.

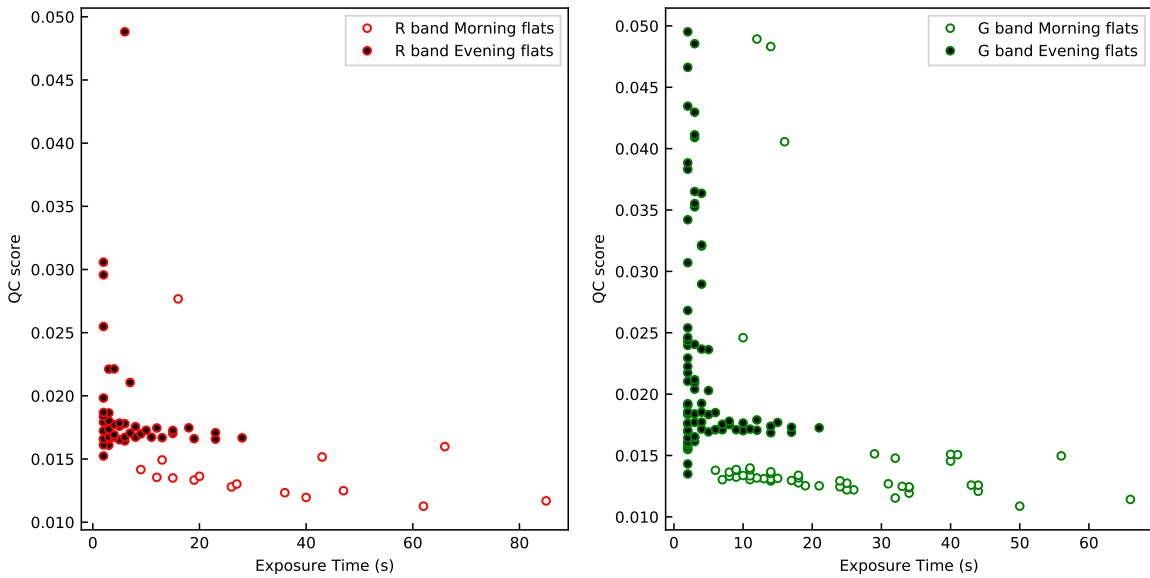


Figure 3.5: Comparison of Flat exposure time and quality control scores across all cameras, split across two panels based on filter type and colour coded based on whether the observation was made in the morning or evening.

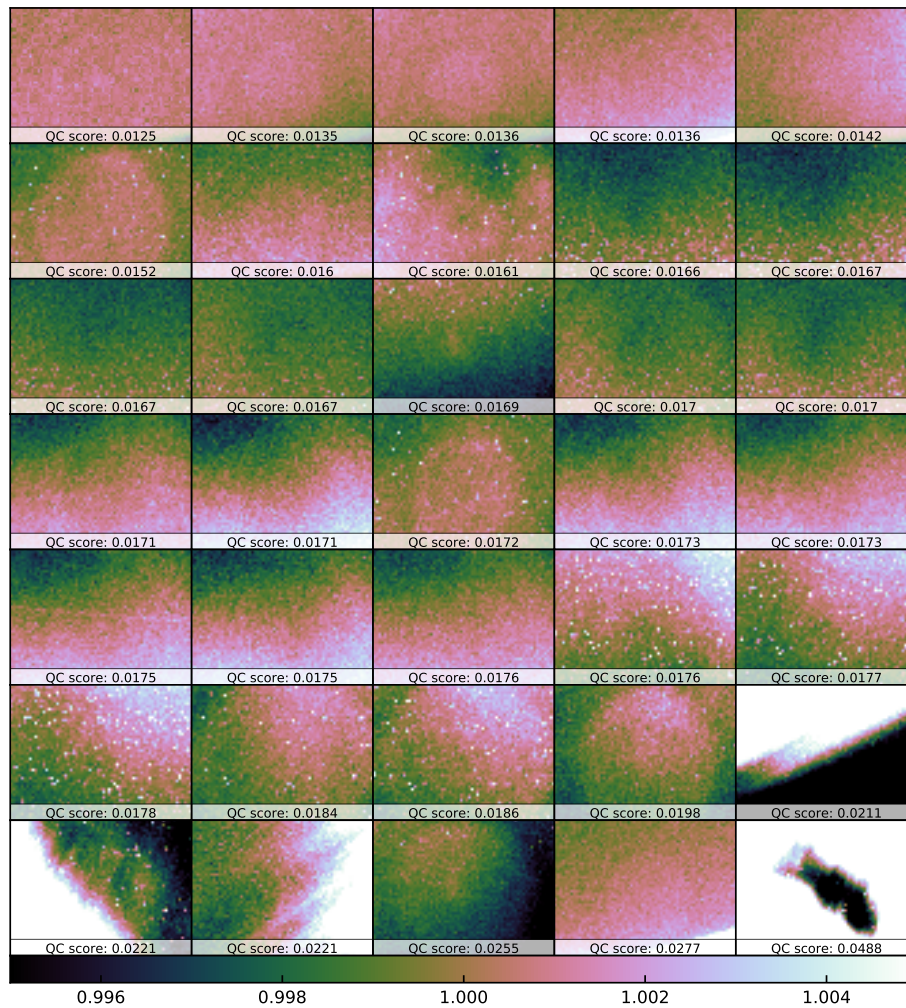


Figure 3.6: A selection of ratios of individual Twilight Flats to a reference master flat, sorted by the QC score. Panels display ratios after  $50 \times 50$  binning to better highlight subtle large scale trends. Recorded at the bottom of each panel is the value of the QC score.

### 3.2.2 Night Flat Quality Control

Quality control for night flats is a considerably more challenging task. While we ultimately assume the night sky provides a flat source of illumination, it is not bright enough for us to feasibly detect the presence of thin cloud as can be done with twilight flats. A promising alternative approach adopted by others and recently described by Zhang et al. [45], is the careful monitoring of the brightness of stars within the frame to determine the quality of observing conditions. The method involves monitoring of what is known as the instrumental zero point, which is an offset term used to correct an instruments measurement of a source (such as a star) with a calibrated quantity in a reference catalogue.

To derive a zeropoint for individual science frames, we first produce a dark subtracted

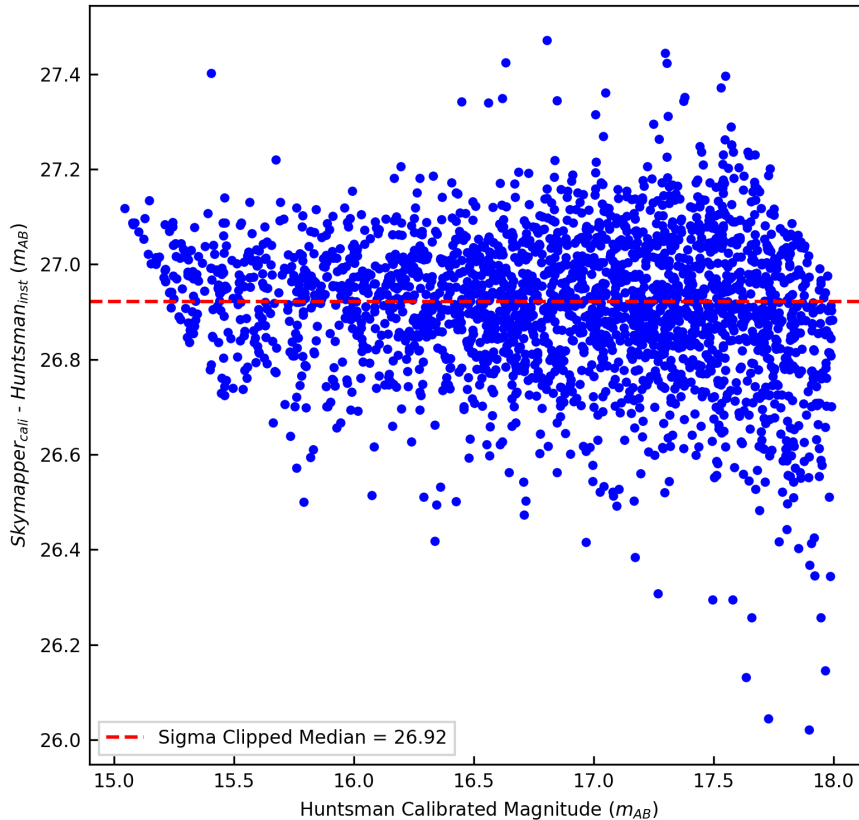


Figure 3.7: Difference of Huntsman instrumental magnitudes and Skymapper calibrated AB magnitudes for point sources in a 5 minute G band exposure. Note, no selection on stellar type was made, so the relatively high intrinsic scatter likely reflects filter differences between the instruments.

and flat-field corrected science frame. We then find sources within the calibrated image and cross reference these the SkyMapper catalogue[44]. SkyMapper has photometric calibration good to  $\sim 1\%$  and covers the entire Southern sky, so is an ideal catalog for deriving Huntsman zeropoints. An initial estimate of the zeropoint can be made by taking the mean of the difference of the SkyMapper and Huntsman instrument magnitude for all sources in the sample. The scatter in these values is large and there are numerous possible causes such as; lack of optimised photometry methodology, galactic dust (further discussed in Section 4.2) and wavelength dependent extinction effects acting on the broad sample of stellar types we are examining. An in depth investigation of the Huntsman photometry is beyond the scope of this thesis. A comparison of this initial zeropoint estimate and the median sky background is presented in Figure 3.8.

These initial zeropoints need to be corrected for atmospheric extinction, as a target field

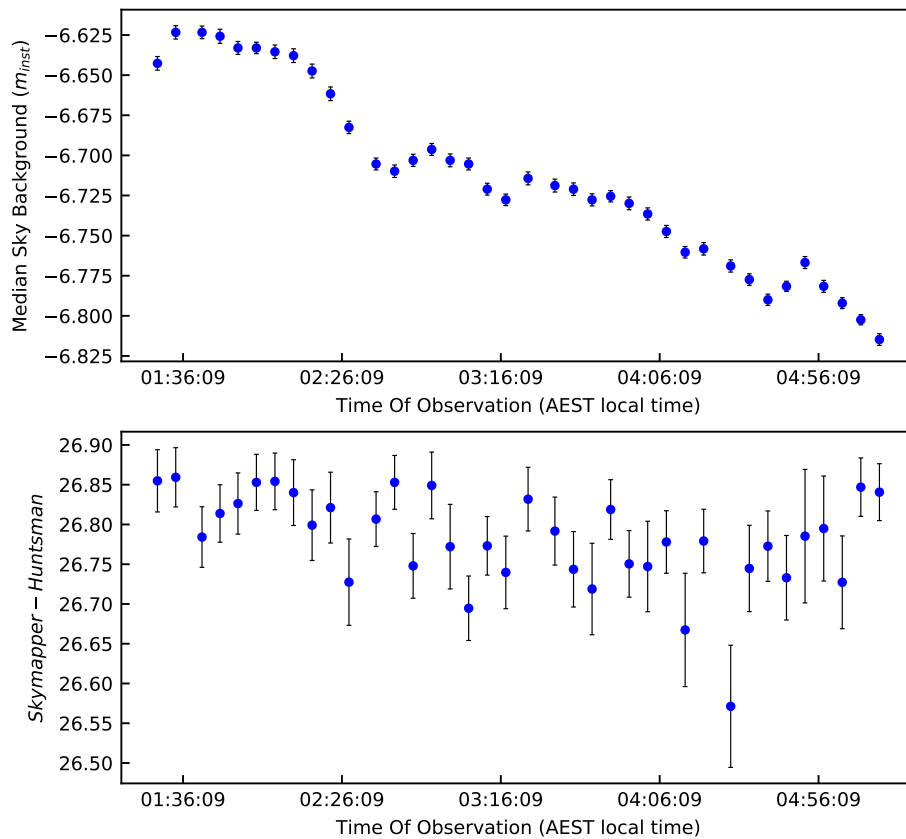


Figure 3.8: A comparison of the median sky background (top panel, measured in Huntsman instrument magnitudes) and the mean of the difference of Huntsman instrument magnitudes and SkyMapper calibrated magnitudes for each frame (bottom panel, an example of which is shown in Figure 3.7). There is a slight correlation between the two, which might be caused by subtle clouds passing through what visually appear to be free of clouds. Error bars are from bootstrap analysis. The observation consisted of tracking a single field over increasing airmass for  $38 \times 5$  minute exposures.

travels over a range of airmasses during a night. The process of correcting for atmospheric extinction is illustrated in Figure 3.9, which shows in the second panel the individual frame zeropoint (measured as already described) for 38 consecutive 5 minute G band exposures. The atmospheric extinction correction is made by performing a linear regression of the difference of the Skymapper and Huntsman magnitudes and the airmass at the time of each observation, as in panel 1 of Figure 3.9. The gradient of this linear fit ( $K_G$ ) gives the atmospheric extinction correction term, while the vertical axis intercept provides the above-atmosphere corrected zeropoint.

The derived atmospheric extinction correction term can be used in conjunction with the

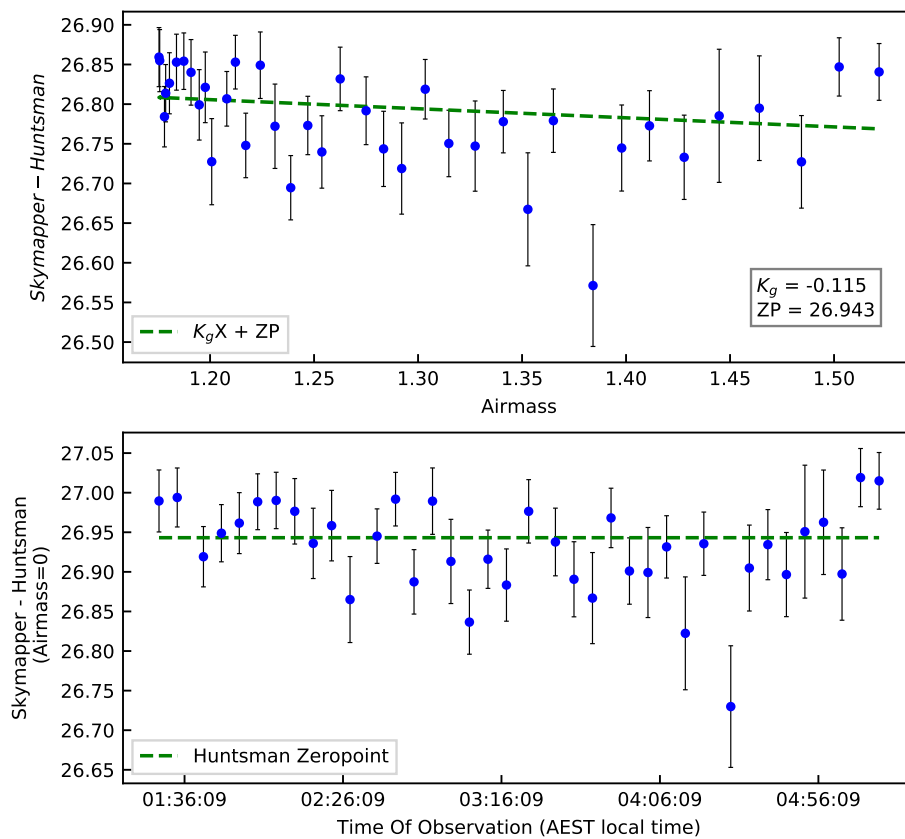


Figure 3.9: The top panel displays the same data as in Figure 3.8, plotted instead against the airmass of the observation. A linear fit was made to the data, providing a calibration of the atmospheric extinction coefficient ( $K_g$ ) and the above atmosphere corrected zeropoint. Using  $K_g$ , it is then possible to correct each observation to an above atmosphere quantity (as shown in the lower panel) allowing a more direct comparison over time.

airmass of each observation to correct the measurements of observation to their above atmosphere values. In the presence of any cloud, the calculated above-atmosphere zeropoint will be inconsistent with the same value determined in clear conditions. These dips in zeropoint are what will in theory allow for quality control of night flats (and science data). According to Zhang et al. [45], the method is very sensitive on the basis that they were able to identify that 25% of their exposures were impacted by what was most likely high altitude ice crystals [10]. The threshold used for identifying these exposures was a deviation of  $\sim 0.1$  mag from the nominal zeropoint.

While no such assessment can be made yet for Huntsman, the establishment of alternative weather monitoring and initiation of regular automatic observing will provided a large data set to evaluation the efficacy of this method.

# 4

## Flat-Field Data Characterisation

Having carried out basic data reduction procedures and implemented quality control strategies in Chapters 2 and 3, we will now characterise the Twilight and Night flats.

### 4.1 Twilight Flat Characterisation

Once a selection of good quality Twilight Flat exposures has been identified, the final processing step is the removal of the twilight gradient. There are two conceivable avenues to achieving this. One requires the use of a night flat, which can be used to disentangle the twilight gradient from the Huntsman vignetting pattern. Once the twilight flat has been divided by the night flat, the gradient can be directly modelled as a tilted plane and subtracted. This combines the benefits of the night flat with the improved noise statistics of the twilight flats [40, 41]. However, to evaluate this method we would first need a night flat so the discussion of this method will be left for Section 4.2.

The second method is to simply average out the gradient by combining morning and

evening flats together, where the final gradient-corrected master flat is simply the average of the morning and evening master. In the analysis below, we keep initially separate the morning and evening flats to explore their overall properties.

In Figure 4.1, a collection of good quality morning and evening G band flats taken with the same camera have been divided by a gradient-corrected master to highlight the difference in gradients with the lens vignetting removed. By sorting by the local time of each exposure we can clearly see the residual morning and evening twilight gradients. The gradients are roughly aligned with the long axis of the CCD, which reflects their orientation relative to the horizon.

It is noticeable that the orientation of the gradients is tending to rotate anti-clockwise with respect to the CCD over the course of the twilight flat windows. In the morning flats, the orientation of gradient changes smoothly along the short axis of the CCD from one corner to another, a rotation of approximately  $75^\circ$ . The evening flats in Figure 4.1 show a similar degree of rotation.

It is implausible that the subtle changing azimuth of the Sun could be the cause of such a dramatic rotation over the 10 minute period over which the flats were taken. A more likely explanation could be that the rotation is produced by the telescope mount. Although twilight observations are made at an azimuth opposing the sun, this must be done by converting to an equatorial coordinate for the Huntsman equatorial mount. The rotation observed in Figure 4.1 could then be the result of rotation about the Right Ascension axis of the mount.

Given the rotational effects it is unclear if a simple averaging of the morning and evening flats will cancel out the gradients. Indeed, in Figure 4.2 the ratio of evening and morning flats is presented and shows a clear residual gradient. Given that we aimed to align the twilight gradients along the long axis of the CCD, the direction of the resulting gradient in the ratio is in line with expectations. Assuming the morning and evening gradients are equal in magnitude, the range in the median ratio values along the pixel columns indicates 0.8% gradient from one edge of the CCD to the other. This is in line with results reported by Chromey & Hasselbacher [9] and Wei et al. [43]. However, if the gradients are misaligned, this ratio will not capture the true range of morning and evening gradient because the maximum or minimum ratio value only tells us the greatest range measured by a single pixel.

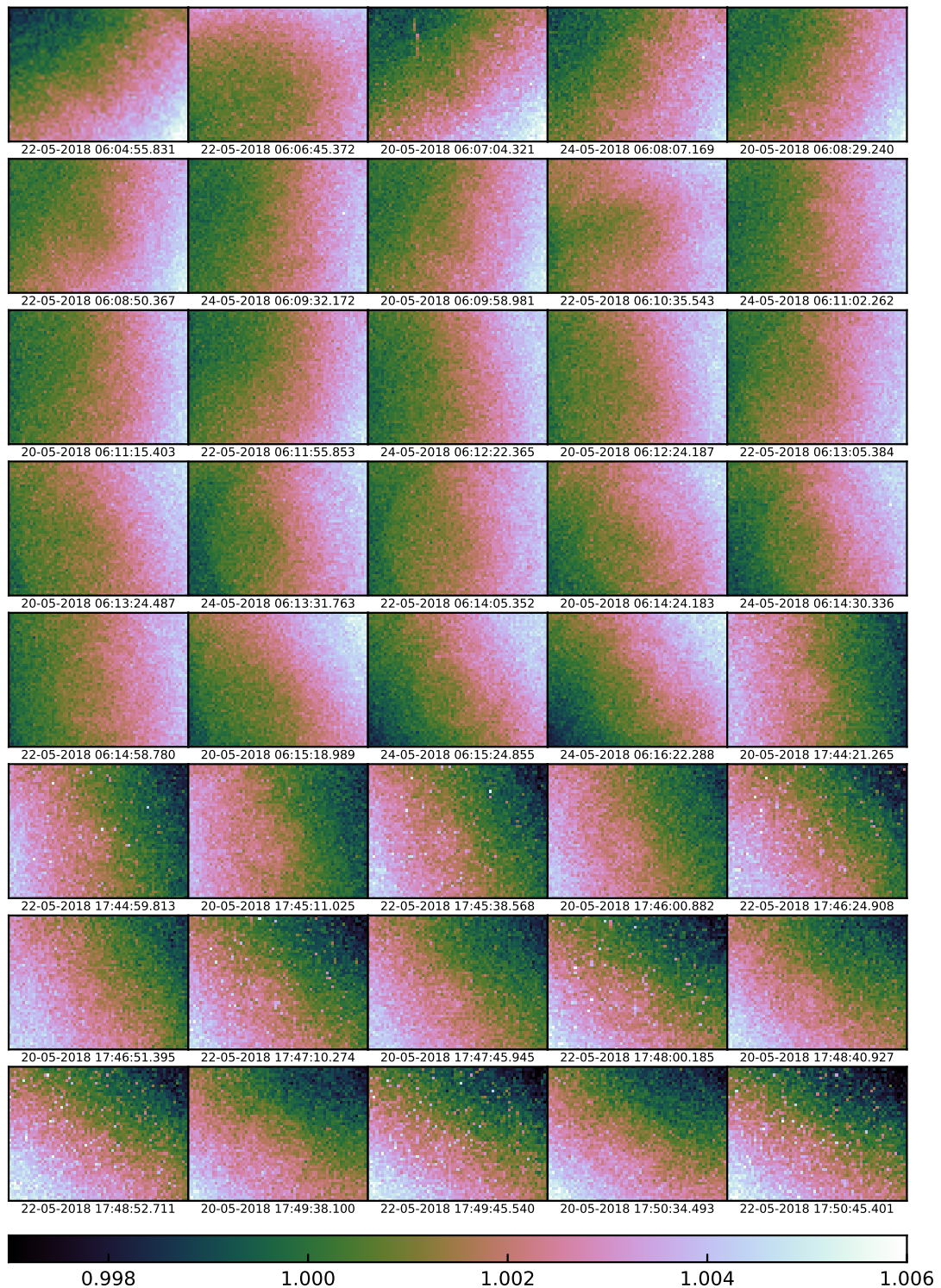


Figure 4.1: Panels show the ratio of an individual morning or evening flat and the gradient cancelled master. The panels have been median binned at a binning scale of  $50 \times 50$  pixels and then sorted by the local time of observation. The data was taken from a single camera (83F010774) with a G band filter.

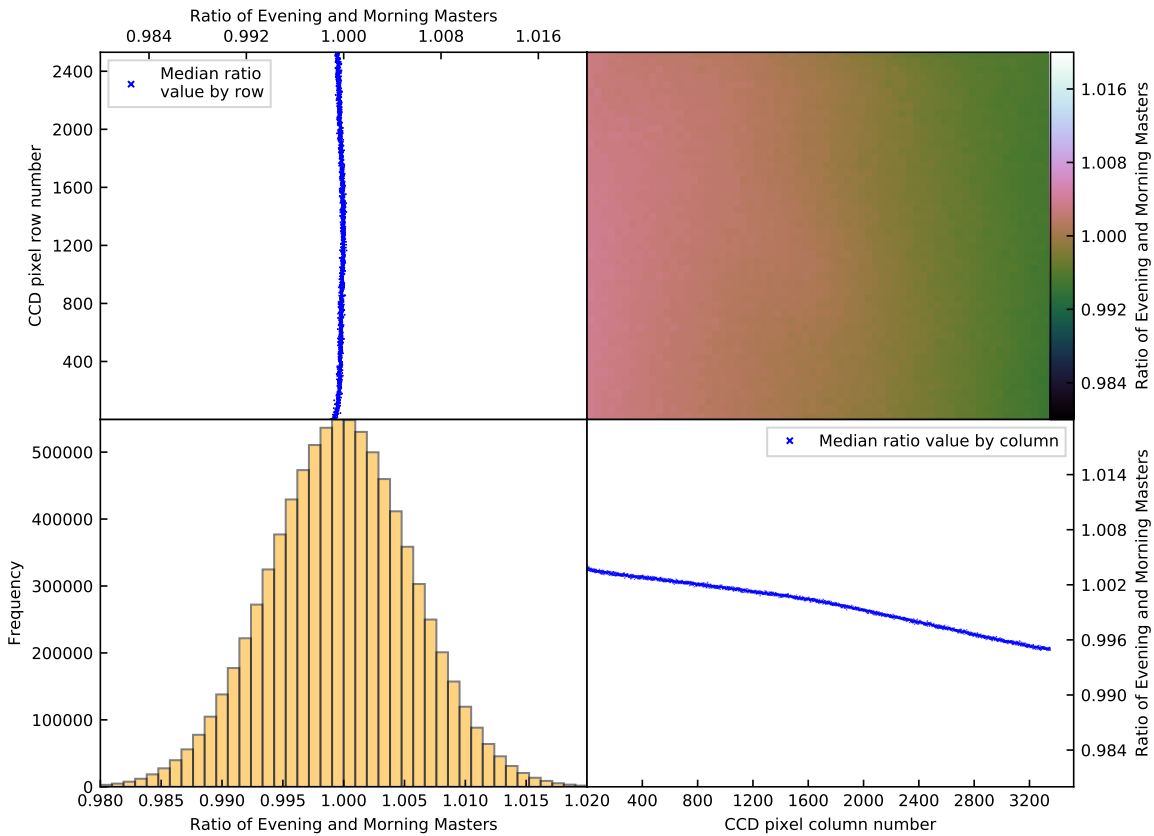


Figure 4.2: Shown from the top right going clockwise: (1) The median ratio value of evening and morning masters, taken along the pixel rows of the CCD, (2) The full ratio of evening and morning masters image, (3) The median value of the ratios taken along the pixel columns of the CCD and (4) The distribution of all ratio values.

#### 4.1.1 Residual Circular Feature

In the process of examining flat to master ratios for the purposes of quality control in Section 1.2 and again while investigating twilight gradients in Section 4.1 something peculiar was noticed. Figure 4.3 shows the modelling and removal of a tilted plane from a single frame's 'flat to master ratio'. The resulting residual shows a rather distinct circular feature that takes up most of the frame.

Features of this nature appear in all good quality flat data as shown in Figure 4.4. The panels in Figure 4.4 have been sorted by local time, which does not appear to correlate with changes in the circular feature. Other versions of this figure sorted by date, exposure time and CCD temperature can be found in Appendix A. No obvious correlation is apparent with any of these factors.

The combination of CCD non-linearity plus the known circular vignetting pattern could

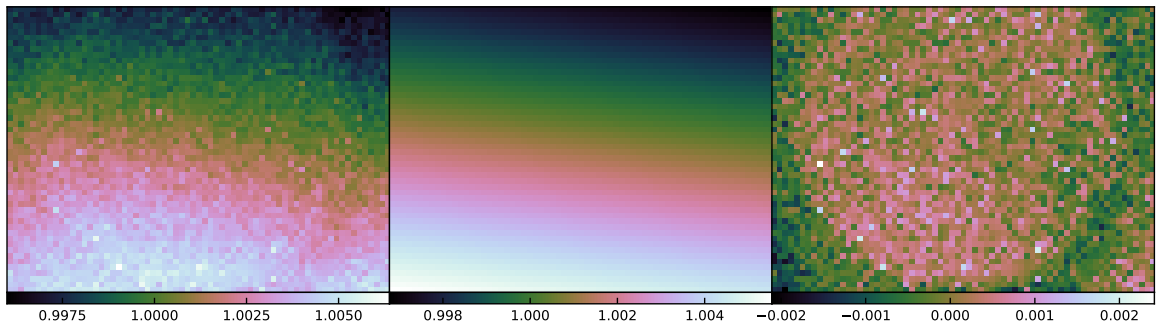


Figure 4.3: Demonstration of the fitting of a tilted plane to a ratio image of an individual flat exposure to a master flat. The subtraction of the gradient helps to identify other forms of large scale deviations of individual flats from their corresponding master flats, including a the distinct circular feature that comes out clearly in the right panel.

feasibly produce circular artifacts of varying radii. However, these flats were taken at count levels well below the regime where non-linearity might emerge (see Section 3.2.1). Furthermore, an artifact produced by non-linearity should produce rings of roughly equal radius, which doesn't appear to be the case. Also a non-linear threshold also would not immediately explain the several instances of multiple concentric rings – only one circular transition region might be expected.

A difference can be noted between R and G band flats, as can be seen in a selection of R band 'flat to master ratio' frames displayed in Figure 4.5. The circular features are less obvious in the R band data, though this might be due to a larger number of noisier evening twilight flats. On the other hand, when examining morning R band flats, similar artifacts of similar magnitude ( $\sim 0.1\%$  fluctuations) are readily apparent.

At present, the cause of the circular feature is unknown, future tests may involve the use of alternative CCDs, filters and optics to isolate a possible internal progenitor. At present, the strength of this feature ( $\sim 0.1\%$  fluctuations) is likely to begin limiting the quality of twilight master flats after combination of 300 or more twilight flat exposures.

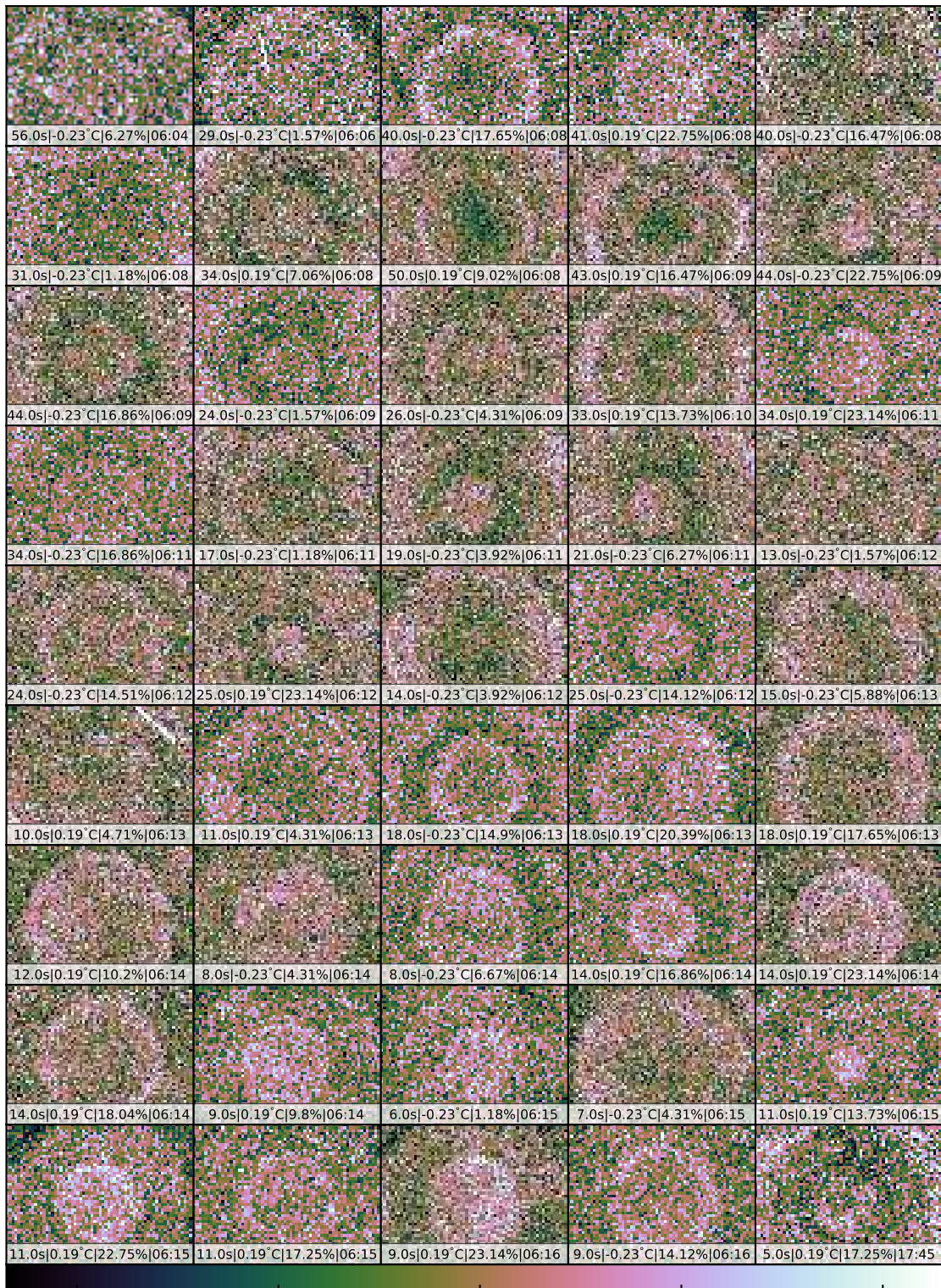


Figure 4.4: Selection of G band flat to master ratios after linear plane subtraction, sorted by local time. Noticeable in all panels is the presence of a centred circular or ring like structure(s) that varies in size and number. At the bottom of each panel the exposure time, CCD temperature and cooling percentage is given.

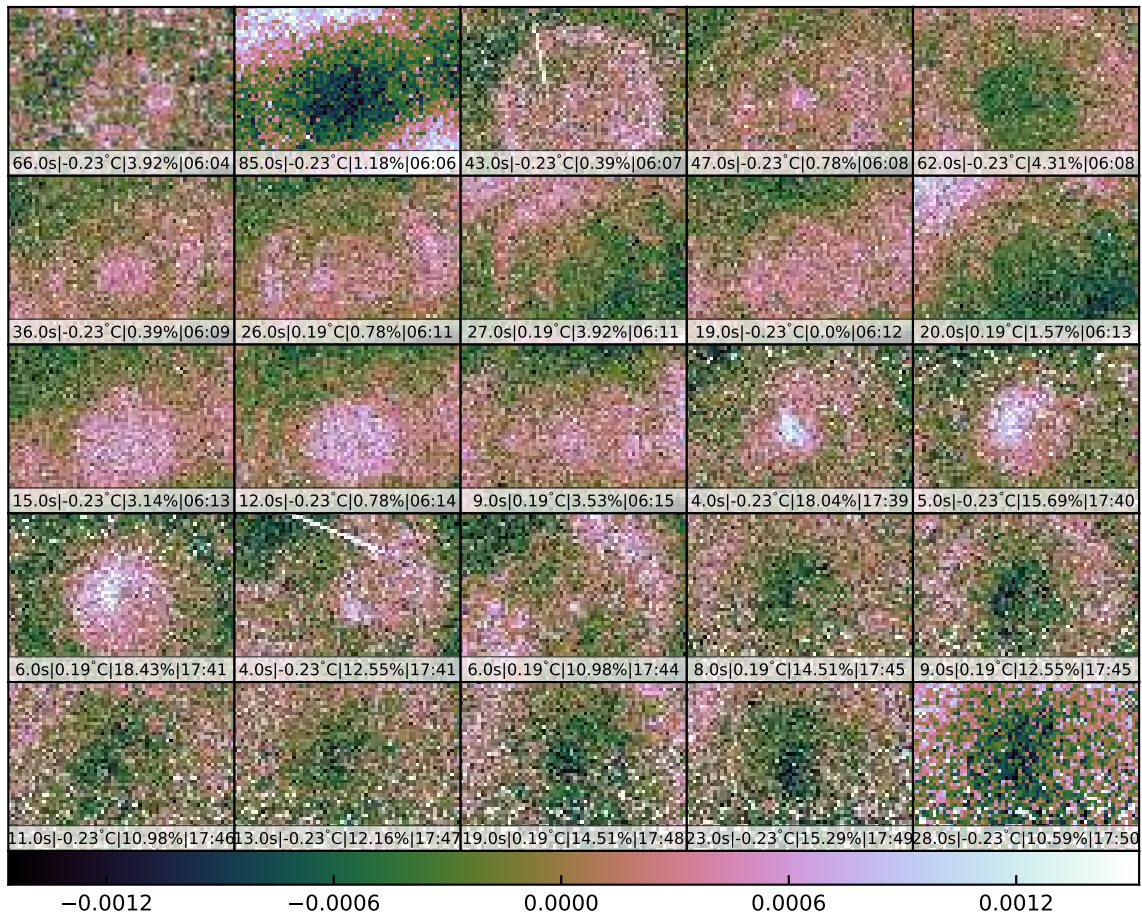


Figure 4.5: Same as Figure 4.4, except for R band flat data. Again, circular features are present in all the data, though the strength of it is less clear due to other structures and increased noise in some of the frames.

## 4.2 Night Flats Characterisation

As outlined in Section 3.1.2, the processing of night flats is broadly similar to processing of twilight flats. Initially effort must be made to ensure the quality of the night flats selected for processing as discussed in Section 3.1.2. Once a set of night flats has been acquired, care must be taken to isolate only the pure night sky contributions in the image. This requires a significant degree of masking. Using the procedure detailed in Section 2.3.2 Figure 2.3, a set of 38 5-minute exposures were masked (the same G band, single night data set was used in Section 2.3.2). The masking fraction in each image was approximately 40%.

In Figure 4.6, the result of stacking the 38 dark night sky flats is presented. While it somewhat captures the vignetting pattern of the system, taking the ratio with a master flat reveals a significant large-scale structure in the master night flat.

Another possibility is that the large-scale structures could be the result of faint emission from the dust within the Milky Way. In Figure 4.7, contours of 100 micron Infrared Astronomical Satellite (IRAS) data [34] are overlaid onto a masked, binned night sky flat. This figure shows that the large-scale structures appear to correlate with regions of enhanced 100 micron emission. By the same argument presented in Section 2.5, a stack of 38 night flats with typical count levels of 500 ADU and 40% masking should produce a master night flat with fractional Poisson noise level of  $\sim 1.6\%$ . However, the standard deviation of the the master night to master twilight flat ratio is indicates 3.1%, almost double what would be expected from Poisson noise alone. This indicates that these night flats are likely being contaminated by low surface brightness emission from galactic dust.

Although dithers were made during these observations, they clearly were not on the scale necessary to compensate for the dust structures seen in Figure 4.7. While a night flat produced from target observations made in this field would certainly not reach the required standard for LSB imaging, it is also true that the field itself would be poorly suited to LSB work. What this data shows is the importance of field selection. Extra care must be taken to ensure target fields are located far from the galactic plane. Even at the Galactic poles it is important to be mindful of regions of enhanced dust emission (from the nearby Inter-Stellar Medium) along the line of sight. Increased dither size would also help in producing a cleaner night flat, by ensuring each pixel is exposed to a more random sample of sky and non sky regions. Assuming the impact of dust could be avoided in this fashion and Poisson noise was again the dominant noise source, a combination of 25 5-minute night flats should produce a master night flat with a QC score (defined in Section 2.5) of less than 0.02.

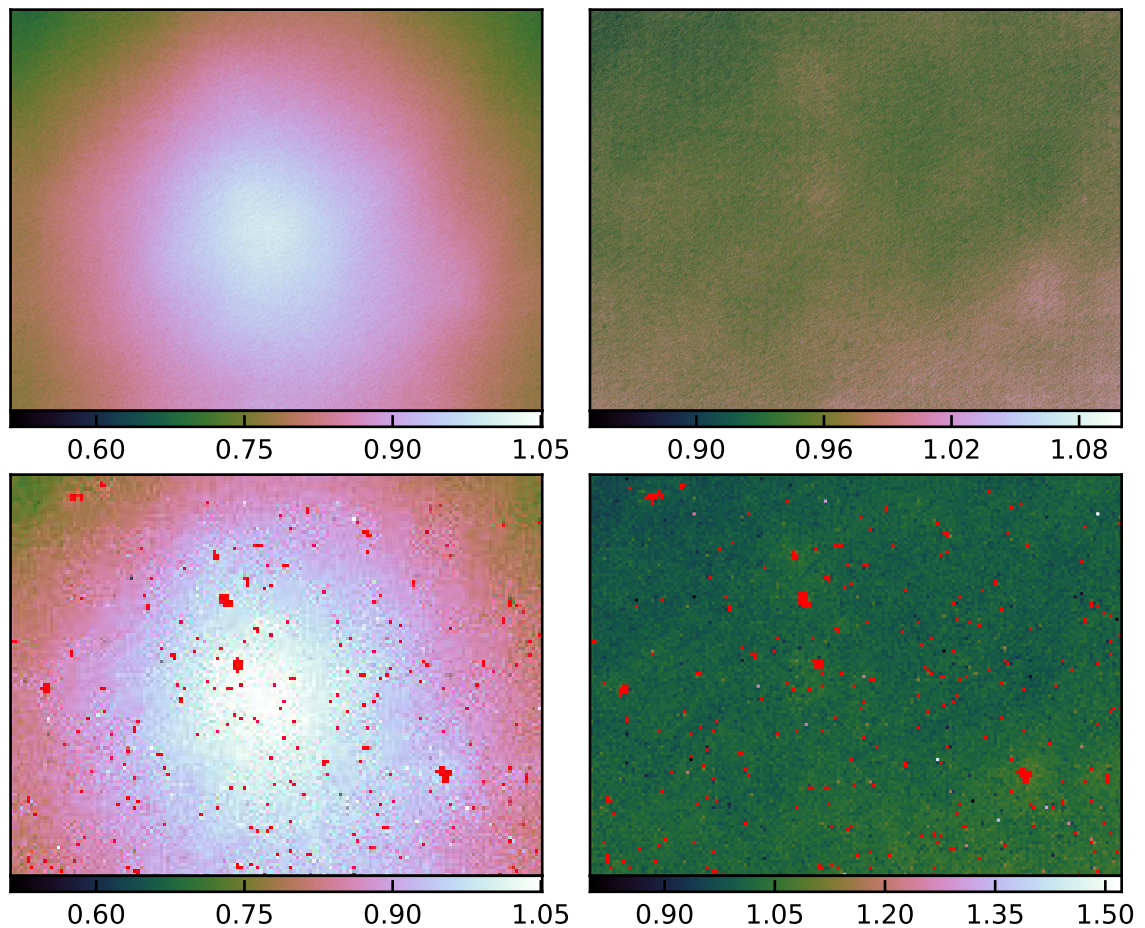


Figure 4.6: From left to right and top to bottom: (1) a master G band night flat produced from a median stack of 38, 5-minute exposures taken with Camera 83F010774; (2) the ratio of this night flat and the corresponding twilight flat for this Camera and filter; (3) A single night flat with mask applied (masked pixels displayed as solid red) and median binned at a scale of  $20 \times 20$  pixels; (4) The previous panel with the master twilight flat correction applied. Unlike twilight flats, the structure in the ratio image is more complex being neither in the form of a smooth gradient, a ring or a circle.

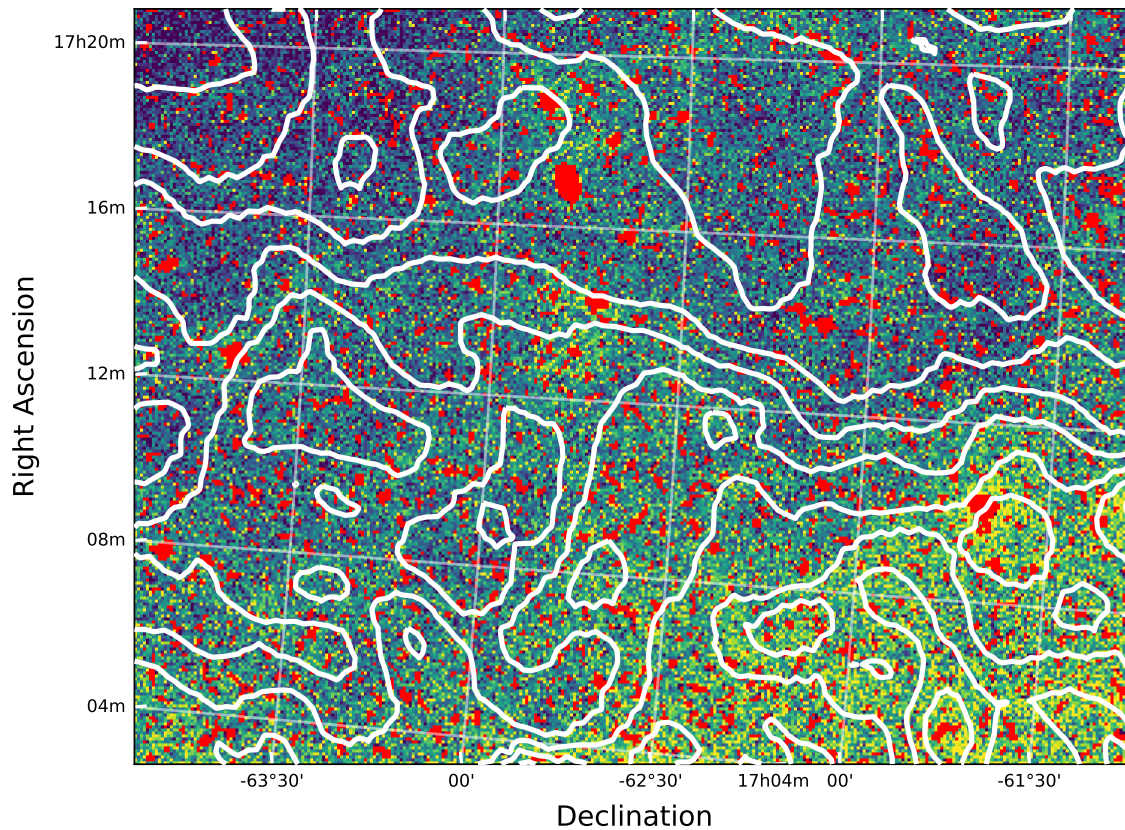


Figure 4.7: A single night flat exposure of 5 minutes taken with Camera 83F010774 with a G band filter. Masked areas are displayed as solid red, the rest of the image shows night background after twilight flat correction and median binning at a scale of  $10 \times 10$  pixels. The white contours are produced from IRAS 100 micron data and are set at ten equally spaced intervals from 6 to  $14.2 \text{ MJy sr}^{-1}$ .

# 5

## Discussion and Conclusions

The key motivation of this thesis is the production of high quality flat-field calibration data to enable the Huntsman Telescope to achieve its low surface brightness imaging objectives. To this end I have examined the two flat-fielding methodologies to make a determination as to what the most suitable approach for Huntsman will be. In the follow sections I will provide a summary of what has been learned and the implications moving forward.

### **5.1 Twilight Flats**

The Huntsman master twilight flats for all camera and filter combinations with a sufficient number of quality observations are shown in Figure 5.1. It is evident that each camera-lens-filter combination contains unique features characteristic of the individual setups.

In order to enable ongoing production of high quality flat calibration data, a reliable method of automated quality control is needed. By considering the expected noise properties of the flats exposures collected, I have been able to implement a simple assessment of flat

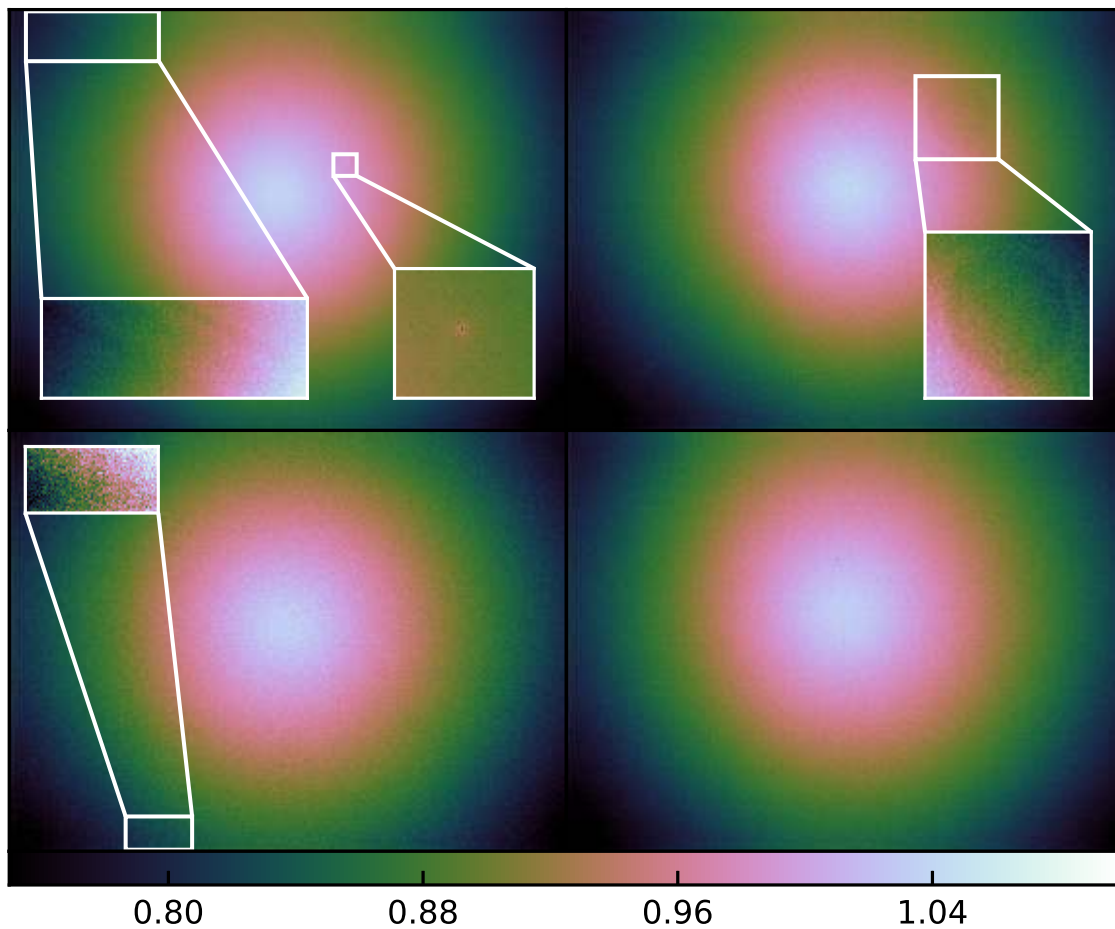


Figure 5.1: Morning and Evening average master flats for: Camera 83F010774 with G band filter (top left), Camera 83F011167 with G band filter (top right), Camera 83F011639 with G band filter (bottom left) and Camera 83F011791 with R band filter (bottom right). Zoomed insets highlight features unique to individual setups, such as faint banding near the edges of the CCD, regions of locally increased sensitivity and circular artifacts.

quality for the purposes of quality control through use of what I refer to as a “QC score” in Section 1.2.

In applying this Quality control screening, I was able to identify a peculiar discrepancy in the quality of data collected between morning and evening. The likely cause is inadequate masking of unfocused starlight in the evening flats, an issue that may not impact the morning data as the focus parameters are well-tuned after a night of observing. One way to verify this is deliberately defocused morning twilight observations and examining its impact on the data quality. Future effort will be made to attempt to focus on bright stars early in evening twilight, before evening twilight data is collected.

As outlined in Section 3.1.3, the main challenge with the twilight flat method is the presence of gradients in the twilight sky over the Huntsman field of view. By examining the ratio of master flats produced from only morning or evening data, it was estimated that the typical gradient across the Huntsman field of view is only 0.2%.

Attempts to cancel out this gradient by combining morning and evening twilight data highlighted a possible issue with this method. The orientation of the gradients appear to undergo a significant degree of rotation over the course of a twilight sequence. It is possible that this rotation is due to tracking of the equatorial mount. Verification of this hypothesis will be made by disabling tracking during a twilight sequence.

In the course of analysing the gradients of the twilight flats I identified the presence of multiple circle or ring-like artifacts in essentially every flat that met quality control criteria. No obvious correlation with various observational parameters could be found with the size or number of the rings and circles. While it was noted that the impact of these artifacts appears less significant in the R band data, this is likely due to the greater proportionate of evening data in the R band flat sample.

To sum up how well twilight flats might be used for LSB imaging, we can take the faintest feature we were not able to easily model and remove and translate it into the limiting surface brightness level due to flat fielding uncertainties. While the rotating gradients in twilight flats complicate modeling, I was still able to successfully remove 0.8% gradients. The remaining dominate feature were the circular artifacts, which are present at the 0.1% level in the flat data. Assuming modelling of these will have some inherent uncertainty due to their complex changes with time, the strength of these features are a conservative limit to estimate the surface brightness floor due to flat fielding. Assuming the 0.1% uncertainty is spread over 300 well-dithered science exposures, Figure 3.1 shows we will be limited to detecting low surface brightness features brighter than  $30 \text{ mag arcsec}^{-2}$  level.

## 5.2 Night Flats

The investigation of Night flats was carried out to explore whether they might provide a useful input for the twilight flats in the event that unsuitable weather prevents the collection of morning or evening twilight flat data on a single night. Assuming that any gradients in the night sky could be averaged out, this would provide an independent measure of the lens

vignetting pattern which could be used to directly model and remove twilight gradients.

As a first step, a quality control procedure that monitors photometric zeropoints was evaluated in Section 2.3.2, which shows hints of a correlation between zeropoint and sky background levels. This is consistent with expectations of light clouds impacting the observations that are otherwise not visually apparent in the images directly. More data are needed to further explore this type of data screening.

Another issue that was explored in Section 2.3.2 is how much object masking impacts night flats. It was found in the field that was analysed, approximately 40% pixels per exposure were masked. Given the typical ADU count per night sky pixel in a 5-minute exposure, it is estimated that a minimum of 25 night flats would be required to produce a single flat field that met the same statistical uncertainty levels as for twilight flats. On a typical 8-hour night of observing, 50-100 science images are expected per camera, so from a statistical point of view, useful night flats should be produced each night.

A master night flat was produced from the data assessed in Section 2.3.2 and compared to a master twilight flat shown in Figure 4.6. Large scale structures were found in the night flat data that are far more significant than what would be expected from statistical noise alone. After a comparison to 100 micron IRAS data in the field, shown in Figure 4.7, it is clear these large scale structures are the result of foreground galactic cirrus. These structures are present at the 3.1% level, which is higher than the uncertainty limits in the twilight data that was analysed. As the field that was analysed was borderline in terms of the average dust extinction level in a suitable Huntsman field (and perhaps not ideal in terms of dust variations across the field), more data is needed to determine if night flats present a viable option.

Another implication of finding the dust structure is that the relatively large dithering pattern of 0.5 degrees adopted for the science data collected for this thesis was not able to average the dust features. This may mean the standard Huntsman observing strategy of observing only 2-3 targets a night will complicate the production of night flats every night, since the dust structures will likely still be apparent even if data from those 2-3 fields are combined. Indeed, even with ideal minimal dust fields, the quality of dark flats will ultimately be limited by low surface brightness dust features, unless a significantly more aggressive dithering scheme is adopted for the science observations.

## 5.3 Future Work

Through the course of this thesis, I have identified several areas for future work. The twilight quality control procedure described in Section 3.2.1 was shown to be effective, however confirmation is needed with larger quantities of data. This will also help understand the variations in quality of morning and evening twilight flats. As suggested, it is likely that the issue is a result of the inability to focus the lenses before evening twilight observations are made.

Quality control for night flats also requires further investigation. Both a comprehensive assessment of optimising the photometric methods and collection of a much larger data set is required to evaluate the usefulness of zeropoint monitoring for Huntsman. If confirmed as an efficient measure of data quality, it will also serve as a valuable quality discriminator for science target data as it was utilised by Zhang et al. [45]. As part of an ongoing zeropoint investigation, further attempts at producing night flats can also be made, preferable in more suitable LSB fields with low and less variable foreground dust extinction.

Perhaps the most interesting avenue of investigation highlighted by this thesis, is the unexpected presence of the circular artifacts in the flat to master flat ratios. These features were only identified after the severe Huntsman vignetting pattern was removed from individual flats. Given the centered and circular nature of these features, it may be possible for them to be modelled in some fashion. However, this process is complicated by the vignetting pattern of the lenses and would likely require an iterative modeling procedure. A crucial initial first step to resolving the issue or modeling and removing the effect, is to identify any kind of correlation that might point to its cause. Ultimately these features are likely to limit stacked Huntsman data to a surface brightness depth of  $30 \text{ mag arcsec}^{-2}$  (See Figure 3.1), so an investigation of them is crucial to Huntsman achieving its Low Surface Brightness Imaging goals.





# Appendix

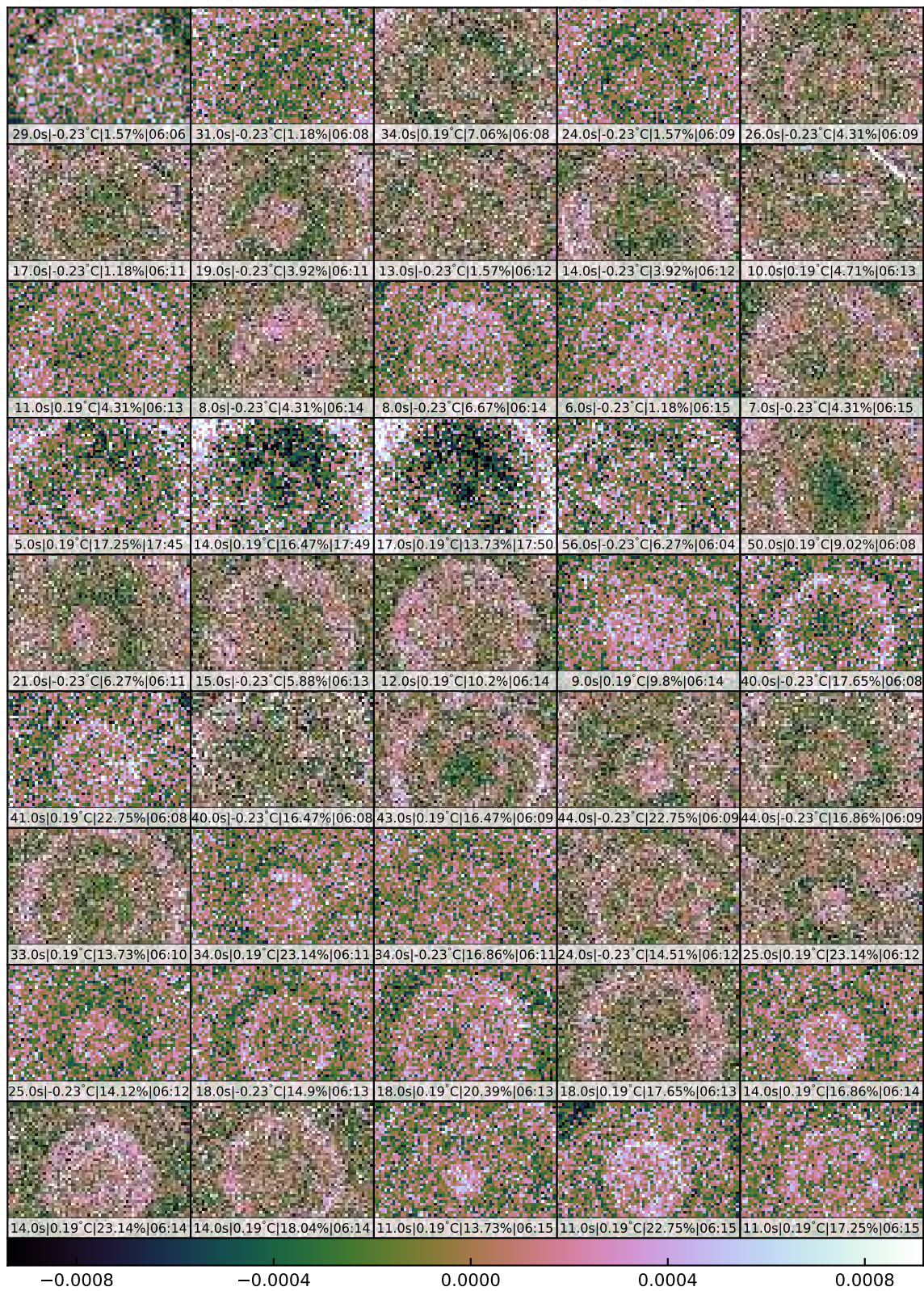


Figure A.1: Figure 4.5 sorted by date.

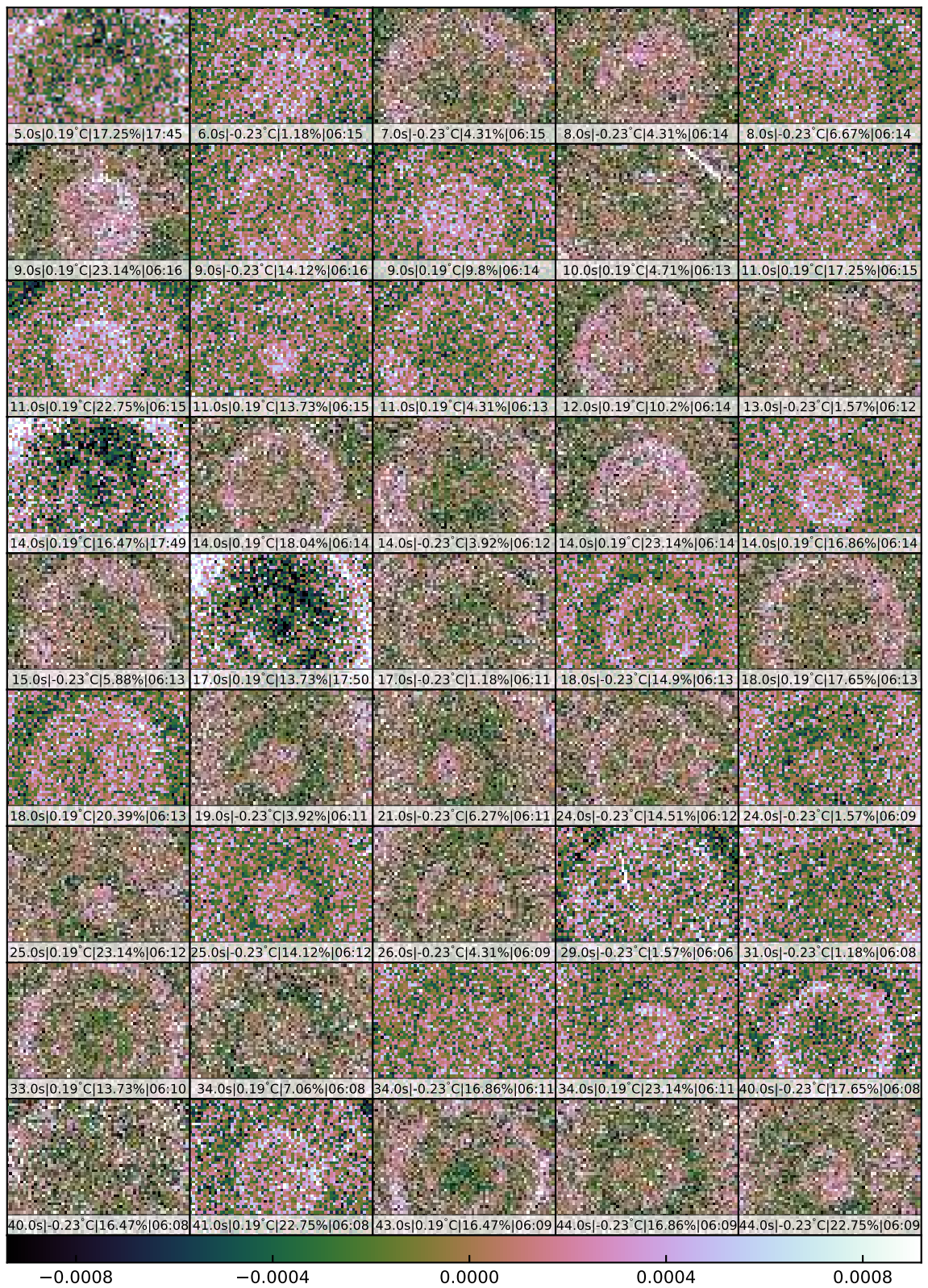


Figure A.2: Figure 4.5 sorted by exposure time.

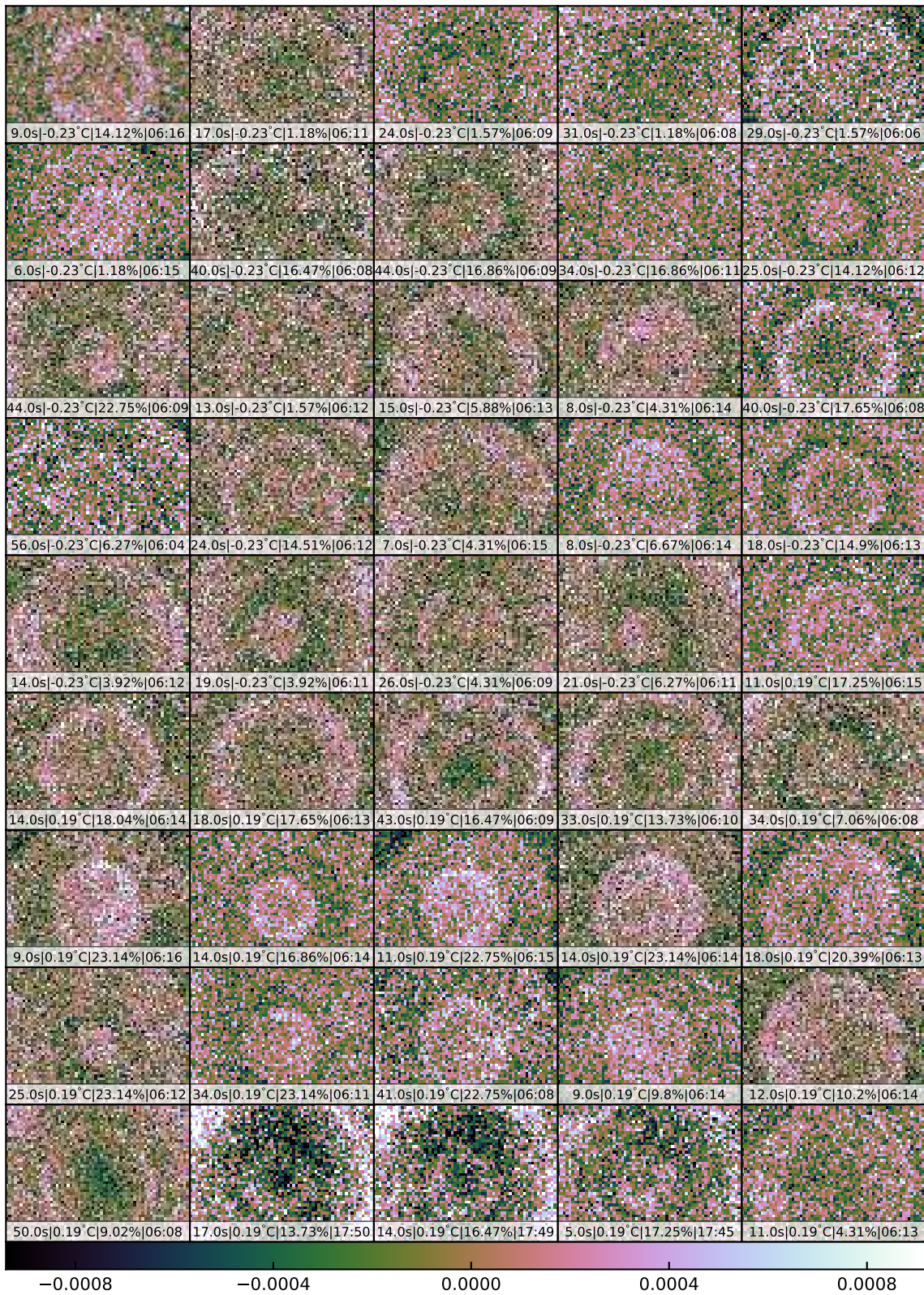


Figure A.3: Figure 4.5 sorted by CCD temperature.



Figure A.4: Figure 4.5 sorted by cooling percentage.

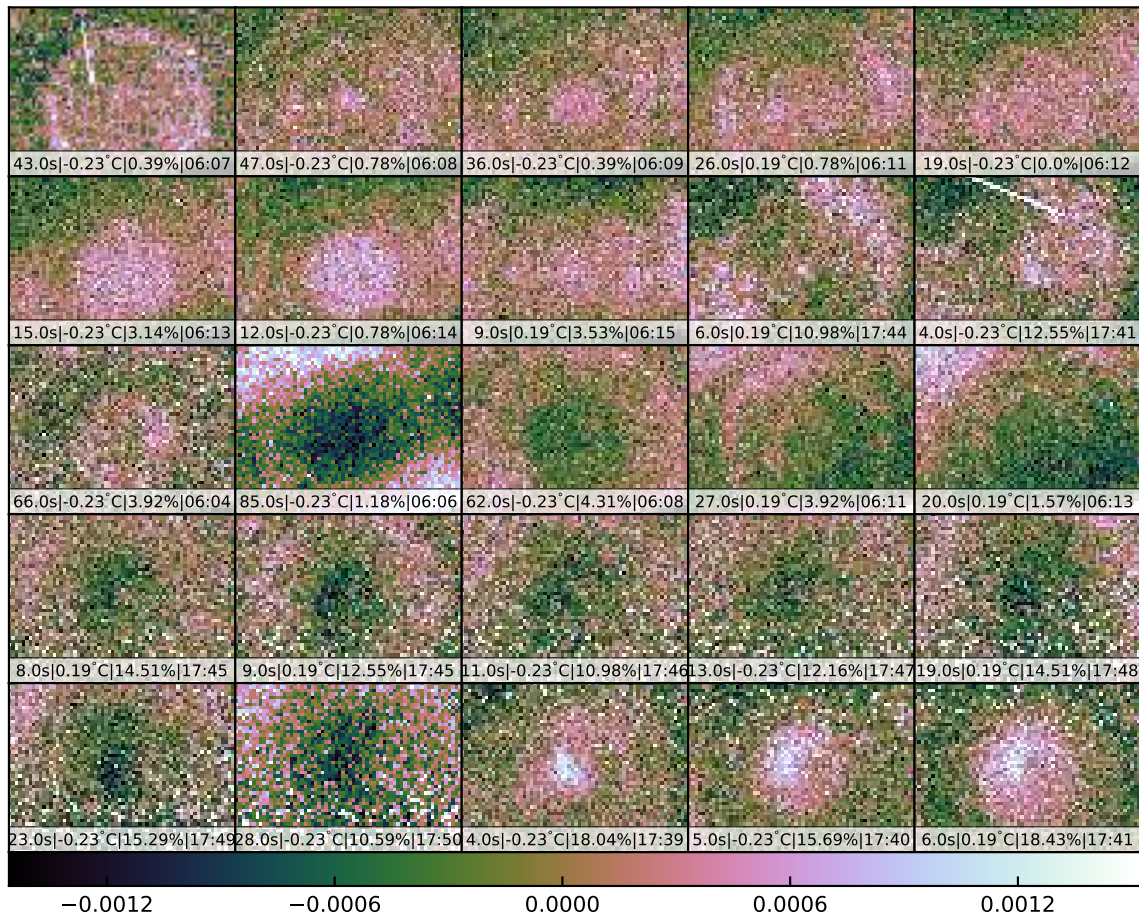


Figure A.5: Figure 4.5 sorted by date.

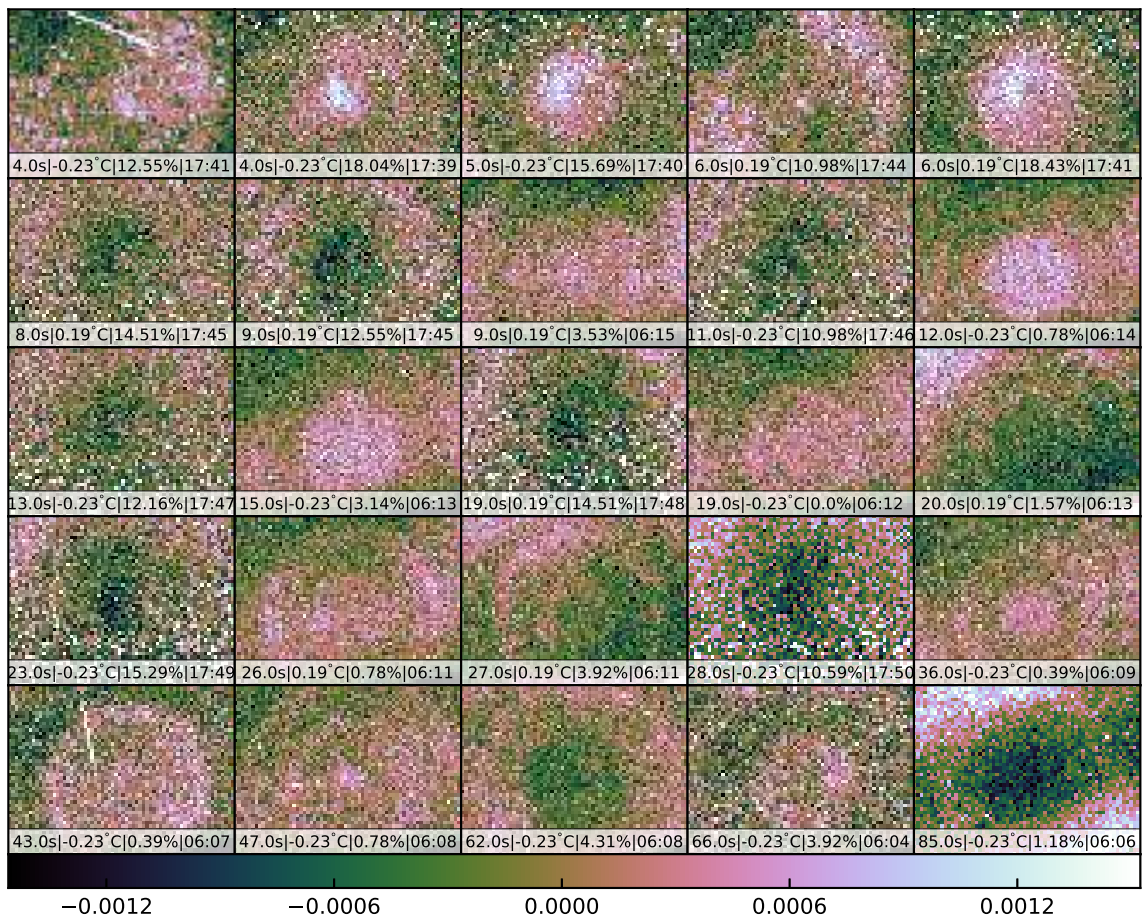


Figure A.6: Figure 4.5 sorted by exposure time.

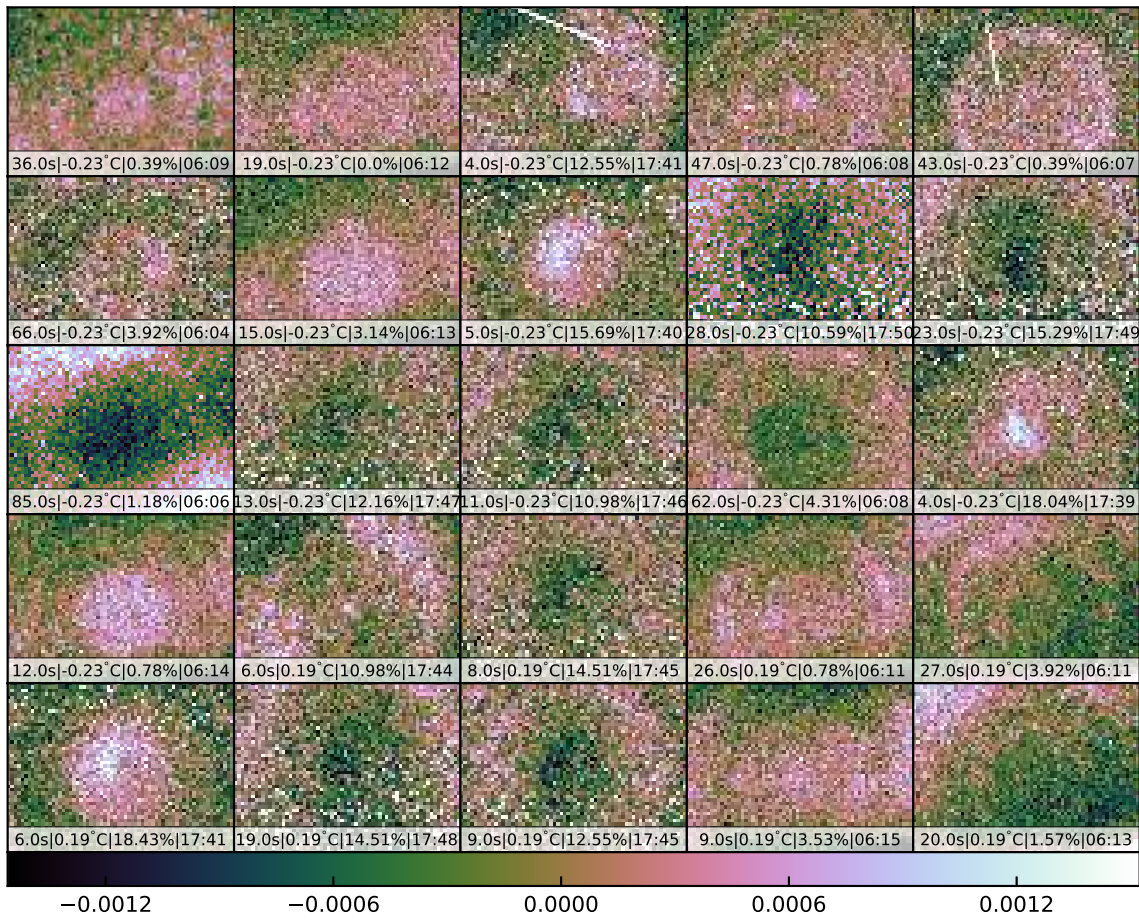


Figure A.7: Figure 4.5 sorted by CCD temperature.

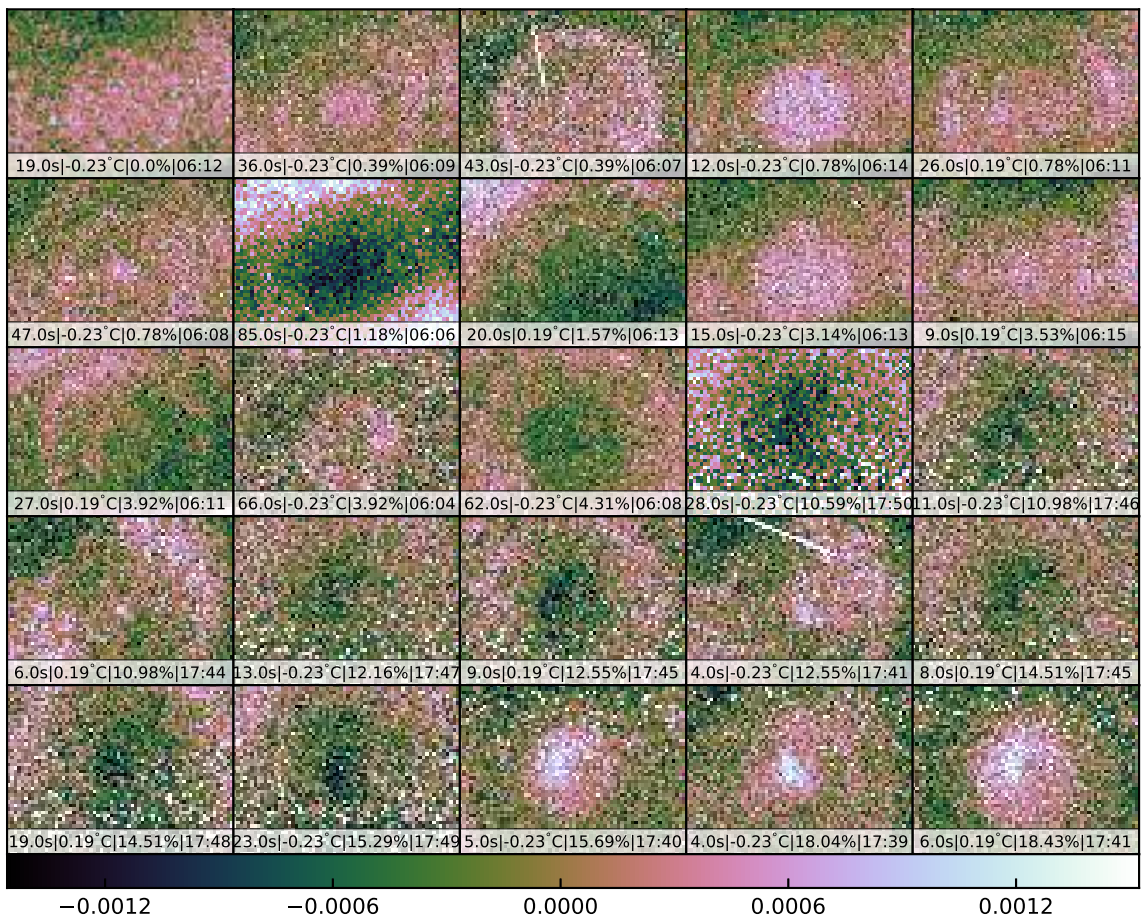


Figure A.8: Figure 4.5 sorted by cooling percentage.



# References

- [1] Abraham R. G., van Dokkum P. G., 2014, *Publications of the Astronomical Society of the Pacific*, 126, 55
- [2] Atkinson A. M., Abraham R. G., Ferguson A. M. N., 2013b, *The Astrophysical Journal*, 765, 28
- [3] Atkinson A. M., Abraham R. G., Ferguson A. M. N., 2013a, *The Astrophysical Journal*, 765, 28
- [4] Bothun G. D., Impey C. D., Malin D. F., Mould J. R., 1987, *The Astronomical Journal*, 94, 23
- [5] Boylan-Kolchin M., Bullock J. S., Kaplinghat M., 2011, *Monthly Notices of the Royal Astronomical Society*, 415, 014
- [6] Bradley L., et al., 2018, *astropy/photutils: v0.5*, doi:10.5281/zenodo.1340699, <https://doi.org/10.5281/zenodo.1340699>
- [7] Bullock J. S., Boylan-Kolchin M., 2017, *Annual Review of Astronomy and Astrophysics*, 55, 343
- [8] Bullock J. S., Kravtsov A. V., Weinberg D. H., 2000, *ApJ*, 539, 517
- [9] Chromey F. R., Hasselbacher D. A., 1996, *Publications of the Astronomical Society of the Pacific*, 108, 944
- [10] Devore J. G., Kristl J. A., Rappaport S. A., 2013, *Journal of Geophysical Research Atmospheres*, 118, 5679

- 
- [11] Duc P.-A., et al., 2015, MNRAS, 446, 120
- [12] Feldmeier J. J., Mihos J. C., Morrison H. L., Rodney S. A., Harding P., 2002, The Astrophysical Journal, 575, 779
- [13] Feldmeier J. J., Mihos J. C., Morrison H. L., Harding P., Kaib N., Dubinski J., 2004, The Astrophysical Journal, 609, 617
- [14] Ibata R. A., et al., 2013, Nature, 493, 62
- [15] Jones E., Oliphant T., Peterson P., et al., 2001–, SciPy: Open source scientific tools for Python, <http://www.scipy.org/>
- [16] Karabal E., Duc P.-A., Kuntschner H., Chanial P., Cuillandre J.-C., Gwyn S., 2017, Astronomy & Astrophysics, 601, A86
- [17] Klypin A., Kravtsov A. V., Valenzuela O., Prada F., 1999, The Astrophysical Journal, 522, 82
- [18] Lamarre J., et al., 2003, New Astronomy Reviews, 47, 1017
- [19] Martínez-Delgado D., Penarrubia J., Gabany R. J., Trujillo I., Majewski S. R., Pohlen M., 2008, The Astronomical Journal, 689, 184
- [20] Martínez-Delgado D., Pohlen M., Gabany R. J., Majewski S., Penarrubia J., 2009, The Astrophysical Journal, 692, 955
- [21] Martínez-Delgado D., et al., 2010, The Astronomical Journal, 140, 962
- [22] Merritt A., van Dokkum P., Abraham R., Zhang J., 2016, The Astrophysical Journal, 830, 62
- [23] Mihos J. C., Harding P., Feldmeier J., Morrison H., 2005, The Astrophysical Journal, 631, 41
- [24] Mihos J. C., et al., 2015, Astrophysical Journal Letters, 809, L21
- [25] Moore B., Ghigna S., Governato F., Lake G., Quinn T., Stadel J., Tozzi P., 1999, The Astrophysical Journal Letters, 524, L19

- 
- [26] Morrison H. L., Miller E. D., Harding P., Stinebring D. R., Boroson T. A., 1997, *AJ*, 113, 2061
- [27] Miller O., Jerjen H., Pawlowski M. S., Binggeli B., 2016, *Astronomy and Astrophysics*, 595, A119
- [28] Miller O., Pawlowski M. S., Jerjen H., Lelli F., 2018, *Science*, 359, 534
- [29] Racine R., 1996a, *Publications of the Astronomical Society of the Pacific*, 108, 372
- [30] Racine R., 1996b, *Publications of the Astronomical Society of the Pacific*, 108, 699
- [31] Rudick C. S., Mihos J. C., Harding P., Feldmeier J., Janowiecki S., Morrison H., 2010, *The Astrophysical Journal*, 720, 569
- [32] Sandin C., 2014, *A&A*, 567, A97
- [33] Sandin C., 2015, *A&A*, 577, A106
- [34] Schlegel D. J., Finkbeiner D. P., Davis M., 1998, *The Astrophysical Journal*, 500, 525
- [35] Slater C., Harding P., Mihos C., 2009, *Publications of the Astronomical Society of the Pacific*, 121, 1267
- [36] Tal T., Van Dokkum P. G., Nelan J., Bezanson R., 2009, *The Astronomical Journal*, 138, 1417
- [37] Trujillo I., Fliri J., 2016, *The Astrophysical Journal*, 823, 123
- [38] Tully R. B., Libeskind N. I., Karachentsev I. D., Karachentseva V. E., Rizzi L., Shaya E. J., 2015, *The Astrophysical Journal Letters*, 802, L25
- [39] Walsh S. M., Willman B., Jerjen H., 2009, *The Astronomical Journal*, 137, 450
- [40] Watkins A. E., Mihos J. C., Harding P., 2015, *The Astrophysical Journal*, 800, L3
- [41] Watkins A. E., Mihos J. C., Harding P., 2016, *The Astrophysical Journal*, 826, 59
- [42] Watkins A. E., Mihos J. C., Harding P., 2017, *The Astrophysical Journal*, 851, 51
- [43] Wei P., Shang Z., Ma B., Zhao C., Hu Y., Liu Q., 2014, *Proceedings of SPIE - The International Society for Optical Engineering*, 9149, 9149

- [44] Wolf C., et al., 2018, Publications of the Astronomical Society of Australia, 35, e010
- [45] Zhang J., Abraham R., van Dokkum P., Merritt A., Janssens S., 2018, The Astrophysical Journal, 855, 78